applied sciences

MDPI

Article

The Geology, Geochemistry, and Origin of the Porphyry Cu-Au-(Mo) System at Vathi, Serbo-Macedonian Massif, Greece

Christos L. Stergiou [1], Vasilios Melfos [1,*], Panagiotis Voudouris [2], Paul G. Spry [3], Lambrini Papadopoulou [1], Alexandros Chatzipetros [1], Katerina Giouri [1], Constantinos Mavrogonatos [2] and Anestis Filippidis [1]

[1] Faculty of Geology, Aristotle University of Thessaloniki, 54124 Thessaloniki, Greece; christer@geo.auth.gr (C.L.S.); lambrini@geo.auth.gr (L.P.); ac@geo.auth.gr (A.C.); agiouri@geo.auth.gr (K.G.); anestis@geo.auth.gr (A.F.)
[2] Faculty of Geology and Geoenvironment, National and Kapodistrian University of Athens, 15784 Athens, Greece; voudouris@geol.uoa.gr (P.V.); kmavrogon@geol.uoa.gr (C.M.)
[3] Department of Geological and Atmospheric Sciences, 253 Science I, Iowa State University, Ames, IA 50011-3212, USA; pgspry@iastate.edu
* Correspondence: melfosv@geo.auth.gr

Abstract: The Vathi porphyry Cu-Au ± Mo mineralization is located in the Serbo-Macedonian metallogenic province of the Western Tethyan Metallogenic Belt. It is mainly hosted by a latite and is genetically associated with a quartz monzonite intrusion, which intruded the basement rocks of the Vertiskos Unit and the latite, 18 to 17 Ma ago. A phreatic breccia crosscuts the latite. The quartz monzonite was affected by potassic alteration, whereas the latite was subjected to local propylitic alteration. Both styles of alteration were subsequently overprinted by intense sericitic alteration. M-type and A-type veins are spatially associated with potassic alteration, whereas D-type veins are related to the sericitic alteration. Three ore assemblages are associated with the porphyry stage: (1) pyrite + chalcopyrite + bornite + molybdenite + magnetite associated with potassic alteration; (2) pyrite + chalcopyrite related to propylitic alteration; and (3) pyrite + chalcopyrite + native gold ± tetradymite associated with sericitic alteration. A fourth assemblage consisting of sphalerite + galena + arsenopyrite + pyrrhotite + pyrite ± stibnite ± tennantite is related to an epithermal overprint. Fluid inclusion data indicate that the A-type veins and related porphyry-style mineralization formed at 390–540 °C and pressures of up to 646 bars (<2.6 km depth) from boiling hydrothermal fluids. A later condensation of vapor-rich inclusions resulted in a moderately saline fluid (8.4–11.2 wt % NaCl equiv) at temperatures between 311 and 392 °C, which were related to sericitic alteration, D-type veins, and associated metallic mineralization. Subsequent dilution of the moderately saline fluid at lower temperatures (205–259 °C) produced a less saline (1.4–2.9 wt % NaCl equiv.) fluid, which is likely associated with the late epithermal overprint.

Keywords: porphyry deposits; Vathi; copper; gold; REE; Serbo-Macedonian metallogenic province; Vertiskos Unit; fluid inclusions

Citation: Stergiou, C.L.; Melfos, V.; Voudouris, P.; Spry, P.G.; Papadopoulou, L.; Chatzipetros, A.; Giouri, K.; Mavrogonatos, C.; Filippidis, A. The Geology, Geochemistry, and Origin of the Porphyry Cu-Au-(Mo) System at Vathi, Serbo-Macedonian Massif, Greece. *Appl. Sci.* **2021**, *11*, 479. https://doi.org/10.3390/app11020479

Received: 10 December 2020
Accepted: 30 December 2020
Published: 6 January 2021

1. Introduction

In northern Greece, the Serbo-Macedonian metallogenic province (SMMP), and the adjacent Rhodope metallogenic province, are part of the Western Tethyan metallogenic belt. Both metallogenic provinces are two of the most promising regions for ore exploration projects in southeastern Europe [1–9]. Throughout the Greek part of the SMMP, several deposits and prospects are enriched in Cu and Au as well as in several critical metals and metalloids, such as Sb, W, Te, Bi, Ga, Co, Ag, rare earth elements (REE; e.g., La, Ce, Gd), and platinum group metals (PGM; e.g., Pd, Pt, Ru) [5,6,10–15] (Figure 1).

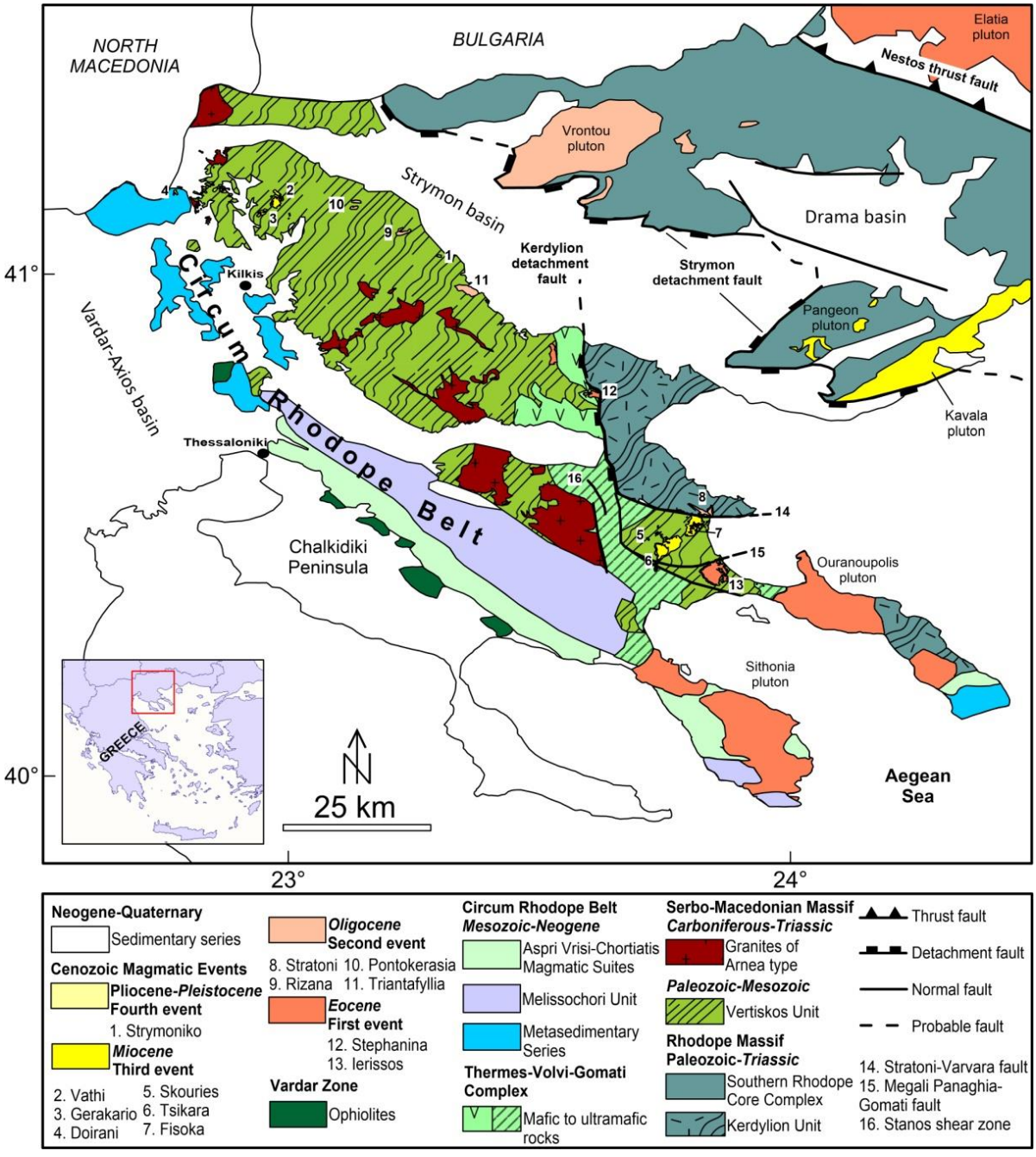

Figure 1. Simplified geological map of the Serbo-Macedonian Massif in northern Greece. The adjacent Kerdylion Unit and the Circum-Rhodope Belt are also shown (modified after [6,16,17]).

The Vathi area is located in Kilkis ore district in northern Greece, which is a poorly explored region containing known porphyry-style deposits in the SMMP (Figures 1 and 2). Preliminary estimates of the resources at Vathi are 15 Mt ore grading 0.30 wt % Cu and 0.8 g/t Au [3,6]. This deposit has been exploited for gold and copper probably during the reign of Alexander I of Macedonia (498–454 BC) [18]. Remnants of surface excavations and galleries are scattered in the area, reflecting the ancient mining activity.

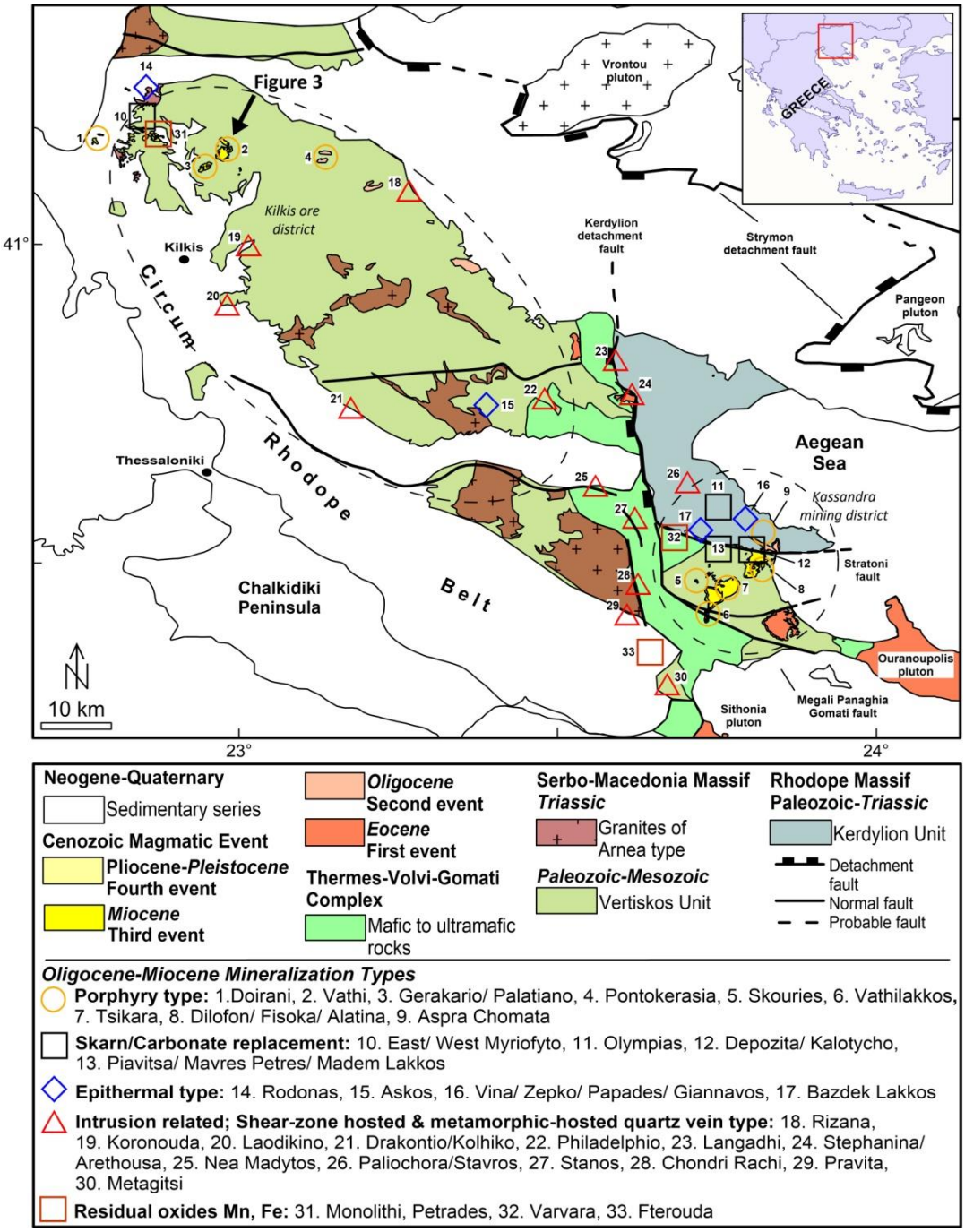

Figure 2. The Cenozoic mineralization of the Vertiskos and the adjacent Kerdylion Units, along with the related magmatic events. The Kilkis and the Kassandra mining district are highlighted. The geological details of Vathi deposit are shown in Figure 3 (modified after [6,13–16,19,20]).

This study focuses on the porphyry system at Vathi and discusses the genetic and spatial relationships among hydrothermal alteration, geochemistry, metallic mineralization, metalliferous distribution, characteristics of the ore-forming fluids, and the structural control on the localization of the deposit. The integrated results of this study are used to discuss the metallogenic processes that formed the mineralization and to establish a genetic model for porphyry-style mineralization in the SMMP.

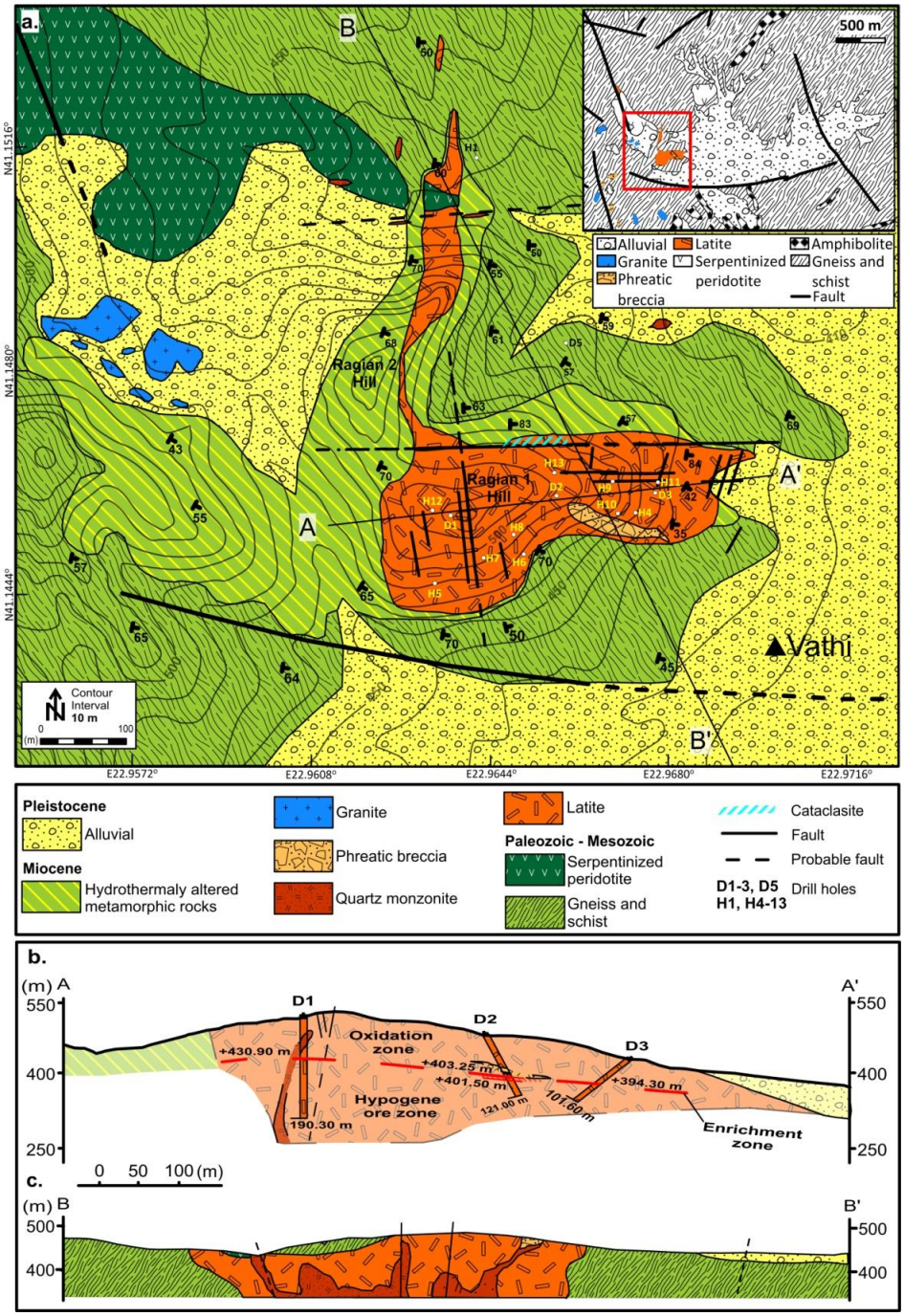

Figure 3. (**a**) Geological map of the Vathi porphyry system. The locations of the legacy drill holes are also shown. Inset map shows the location of the Vathi magmatic rocks in respect to local geological settings; (**b**) Schematic cross-section A-A′ of Ragian 1 Hill, defined by Institute of Geology and Mineral Exploration (IGME) drillings and drill core interpretation. Drill holes D2 and D3 were inclined; (**c**) Schematic cross-section B-B′ of Ragian 1 Hill. Interpretation was based on field mapping held during this study and on observations made by Melidonis (1968) and Markoulis (1970).

2. Geological Setting

The Serbo-Macedonian Massif (SMM) in Greece is represented by the Vertiskos Unit that is composed of the following: (i) a sequence of migmatites, gneisses, schists, and thin marble intercalations, and (ii) a sequence of metagabbros, metadiabases, and amphibolites, intercalated with gneisses [17,21–24]. Mafic to ultramafic rocks which belong

to the Thermes-Volvi-Gomati complex, are tectonically emplaced in these sequences [25] (Figure 1).

Abbo et al. [26] describes three pre-Alpine pulses and one Cenozoic magmatic pulse related to the igneous evolution of the Vertiskos Unit. Neoproterozoic and middle Ordovician granitoids metamorphosed into orthogneisses, and A-type granites (so-called Arnea-type granites) characterize the pre-Alpine igneous evolution [22]. The Cenozoic magmatism is subdivided into four magmatic events [16,22,26] (Figure 1). These magmatic events include I-type plutonic rocks, and related subvolcanic and volcanic rocks with calc-alkaline to high K-calc-alkaline and shoshonitic affinities, which intruded the SMM and the neighboring Rhodope Massif mainly as late-stage intrusions [27–29].

The first Cenozoic magmatic event (Early to Middle Eocene) is characterized by intrusions unrelated to metallic mineralization [16,20,28–30]. The second event formed during the Oligocene, and it is associated with mineralized intrusions. During this event, calc-alkaline magmatism was produced following an E-W trend [29] (Figure 1). The third event started in the Early Miocene (22–17 Ma) and is characterized by the intrusion of several subvolcanic rocks that host porphyry-style mineralization (e.g., Vathi, Gerakario, Skouries, and Fisoka) [16,20,31]. The last magmatic event (Pliocene to Pleistocene) is not related to mineralized intrusions and it is mostly restricted to the Strymoniko rhyolitic dome [19].

The rocks of the Vertiskos Unit were affected by two metamorphic events: (i) a Cretaceous amphibolitic facies and (ii) a Cretaceous to Early Paleogene event related to local retrograde greenschist facies [17,22].

Two extensional events were reported by Kilias et al. [21]. The oldest is contemporaneous with the Cretaceous amphibolite facies metamorphic event and exhibits an ENE-WSW extensional trend and eastward-trending shears. The youngest extensional event occurred during the Late Cretaceous and Middle Eocene (68.5 $\pm$ 3.8 to 46.6 $\pm$ 3.6 Ma) and continued through to the Miocene [21,32,33]. The faults of this event structurally controlled the intrusions related to the second and the third Cenozoic magmatic events [19,20].

3. Oligocene-Miocene Ore Deposits and Prospects of the Serbo-Macedonian Metallogenic Province (SMMP) in Greece

The SMMP and Rhodope metallogenic provinces contain several ore deposits and prospects of Cenozoic age [5,6,8,34–37]. According to Kockel et al. [19], 48 ore deposits (e.g., porphyry, epithermal and replacement types) occur in the Vertiskos Unit and the adjacent Kerdylion Unit that are genetically associated with the Oligocene-Miocene magmatism (Figure 2). These deposits and prospects occur mainly in the Kilkis ore district to the north and in the Kassandra district (NE Chalkidiki) to the south [6,19,20,38,39].

The Kilkis district hosts porphyry (e.g., Pontokerasia, Vathi, Gerakario), skarn/carbonate replacement (e.g., East and West Myriofyto), and epithermal-type (Rodonas) mineralization (Figure 2). A calc-alkaline syenite and a granodiorite intrusion host the Gerakario Cu-Au-Sb porphyry–epithermal deposit, whereas the Pontokerasia Cu-Mo-Au porphyry deposit is spatially associated with a calc-alkaline syenite intrusion [16]. Preliminary estimations of resources based on old exploration data for the Gerakario, Pontokerasia, and Vathi porphyry deposits indicate more than 258 Mt of ore with 0.40 wt % Cu and 0.9 g/t Au [3].

The Kassandra mining district in NE Chalkidiki is one of the oldest mining districts in Europe [6]. Several porphyry (e.g., Skouries, Fisoka), epithermal (e.g., Vina), and skarn/carbonate replacement (e.g., Olympias) deposits and prospects are distributed in an area of approximately 480 km^2 [6,8,20,38] (Figure 2). Most of these deposits are spatially associated with intrusions that were emplaced in a narrow belt at an extensional tectonic setting, which is localized by the Kerdylion detachment fault and the Stratoni and Megali Panaghia-Gomati normal to oblique faults [30]. The proven and probable resources of the NE Chalkidiki area include approximately 951 Mt grading 7.76 g/t Au, 273 g/t Ag, 0.49% Cu, 10.1% Pb, and 13.7% Zn [39].

Additionally, several deposits occur that are not spatially associated with any intrusive or extrusive magmatic rocks. These deposits include shear-zone hosted vein-, metamorphic-

hosted quartz vein-, and epithermal-type deposits [11–13,40,41] (Figure 2). The polymetallic Laodikino and Stanos Cu-Au-Sb-Bi-Te quartz vein deposits are hosted in shear zones, and the Rizana vein-type Sb prospect (active underground mining until the late 1950s produced 22.5 Mt of ore grading up to 40% Sb) are typical examples of these deposits and prospects [12,13,41].

4. Local Geology

The main crystalline rocks in the Vathi area include Paleozoic two-mica gneisses, schists and amphibolites of the Vertiskos Unit (Figure 3a–c), which were metamorphosed to the amphibolite facies [42]. The gneiss include quartz, plagioclase (An = 25–30%), K-feldspars, biotite, and muscovite, while garnet, epidote, and titanite occur in minor amounts [42]. The schist consists of quartz, muscovite, biotite, and plagioclase, and it is intercalated with the gneiss. Amphibolite and amphibolitic schist occur in lenses and consist of plagioclase, hornblende, titanite, epidote, and minor pyroxene [42]. These metamorphic rocks trend NNE-SSW and dip ESE at ~65° [42]. Unmineralized pegmatites and milky quartz veins crosscut the metamorphic rocks, whereas thin quartz lenses occur occasionally, and they are parallel to the schistosity of these rocks.

A serpentinized Paleozoic–Mesozoic peridotite is intercalated with the gneiss at the northwest of the study area (Figure 3). It consists of olivine and pyroxene that were replaced by serpentine and talc, with magnesite veins crosscutting the rock [42]. Magmatic rocks that host the Vathi mineralization comprise subvolcanic stock-like bodies and dikes exhibiting porphyritic texture that intruded the crystalline rocks [16,42]. Two rock types are distinguished: a latite, extending from Ragian 1 Hill to part of Ragian 2 Hill, and a quartz monzonite outcropping to the north of Ragian 2 Hill (Figure 3a and inset map).

The latite at Vathi forms an oval shaped plug covering an area of ≈0.25 km^2 at Ragian 1 Hill, with a narrow 400 m long apophysis trending toward the north (Figure 3a). Geophysical investigation reveals that the latite dips to the east to a depth exceeding 240 m [43]. Melidonis [42] and Andronopoulos [44] characterized this intrusion as rhyodacite, whereas Frei [16] referred to it as latite. At the surface, small oval-shaped outcrops of quartz monzonite trend E-W and intrude the basement rocks and the latite [45] (Figure 3a and inset map). Frei [16] obtained two U-Pb zircon emplacement ages of 18 ± 0.5 Ma and 17 ± 1 Ma.

An ESE-WNW trending phreatic breccia, approximately 120 m long, 25 m wide, and more than 10 m thick at the surface, intrudes the latite along the eastern part of Ragian 1 Hill (Figure 3a). In addition, more breccias are found southwest of Ragian 1 and 2 Hills (Figure 3; inset map).

West and southwest of Ragian 1 and 2 Hills, small barren intrusions of biotite granite and amphibole granite occur (Figure 3a and inset map). These rocks are slightly affected by sericitic alteration. The formation of these rocks was contemporaneous to the subvolcanic intrusions [42]. Tectonically, Vathi lies in a graben bounded by faults with WNW-ESE and E-W trends (Figure 3; inset map). Quartz monzonite and the latite are located near the intersection of two of these faults (Figure 3). Local faults along Ragian 1 and 2 Hills reflect these regional structures (Figure 3). In addition, a group of NE-trending structures is observed. The NE-trending structures strike N52E and dip 51° to NW, while the NW-trending structures strike N25W and dip 60° to ENE. The E-trending structures strike N76E and dip 70° to SSW.

The magmatic and hydrothermal activity within the Vathi porphyry system is genetically and spatially associated with these faults and structures (Figure 3). The quartz monzonite occurs in narrow, elongated intrusions which trend E-W. The mineralized phreatic breccia intrudes the latite along an almost E-W direction (Figure 3).

Along the northern part of Ragian 1 Hill, a group of structures is present that trends E-W, which is accompanied by several minor conjugate NE-SW structures (Figure 3). Locally, along these E-trending structures, in the latite, a cataclasite is found. Veins, in places as sheeted veins, are associated with the E- and NE-trending group of structures and dip 60° to 76° toward SSW. They occur on the northeastern side of Ragian 1 Hill

(Figures 3 and 4). At this site, an ancient gallery, approximately 1 m wide, was opened along these veins possibly for gold and/or copper exploitation (Figure 4).

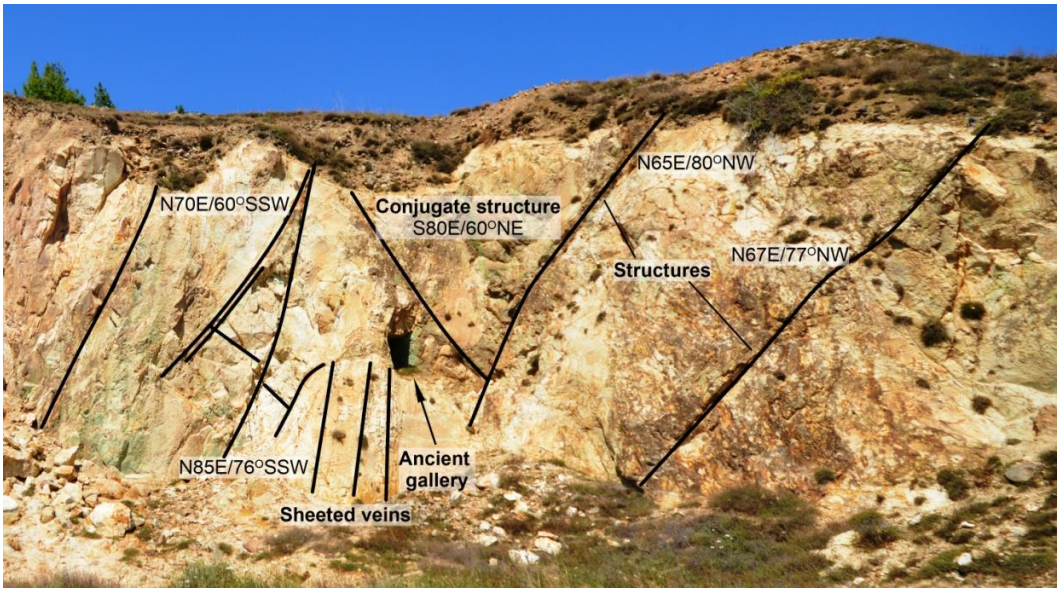

Figure 4. Veins, locally sheeted, containing supergene mineralization with minor quartz and sericite that are associated with E- and NE-trending structures and which crosscut latite at the eastern side of Ragian 1 Hill.

5. Methods

The studied mineralization (N41.1458°, E22.9639°) is located northwest of the Vathi village in the Kilkis area and spans two hills, Ragian 1 Hill and Ragian 2 Hill (Figure 3a). Surface geological mapping and sampling resulted in the collection of 43 mineralized surface and hydrothermally altered samples from the igneous and surrounding metamorphic rocks. Geological mapping collected information on lithologies, lithological boundaries, and structural relationships. In addition, samples from legacy drill cores were obtained along with previously acquired logging data.

These legacy drill cores were collected in the late 1960s and early 1970s during an exploration program that was targeting uranium-bearing mineralization in the area. The Institute of Geology and Mineral Exploration (IGME) of Greece conducted an exploration drilling project during 1968. Two vertical drill holes (D1, D5; Figure 3a,b) and two inclined drill holes (D2, D3; Figure 3a,b), 512.90 m in length were drilled [46], with the results of geological mapping and geophysical exploration being reported by Melidonis [42], Thanasoulas [43], and Andronopoulos [44]. A further exploration drilling program was carried out by Bauxites Parnasse Mining Co. S.A. to target porphyry copper-style mineralization. This program included 11 vertical drill holes (H1, H4-13). Eight polished sections were made from drill core H4, between 43 and 166 m, with seven additional polished sections being made from drill core H5, between 53 and 73 m (H4, H5; Figure 3a).

Optical microscopy was conducted on 44 thin, polished, and polished-thin sections from the surface samples along with the samples obtained from drill cores, using a Leitz Laborlux 11 Pol S dual reflected-transmitted light polarizing microscope. Scanning electron microscope (SEM) studies of oxidized rock samples were conducted at the Faculty of Sciences, Aristotle University of Thessaloniki, using a JEOL 840 SEM equipped with an ISIS 300 OXFORD energy-dispersive spectrometer (EDS). Twenty-one samples of mineralization and the host rocks were analyzed for major and trace elements, including rare earth elements, by X-ray fluorescence (XRF), and inductively coupled plasma-mass spectrometry (ICP-MS) at ACME Laboratories, Vancouver, Canada.

Fluid inclusions were studied in five doubly-polished wafers of quartz in veins containing metallic minerals. A LINKAM THM-600/TMS 90 heating–freezing stage coupled to a Leitz SM-LUX-POL microscope was used for the microthermometric measurements at the Department of Mineralogy, Petrology, Economic Geology, Aristotle University of Thessaloniki. Ice (H_2O) and organic reference substances with known melting points were used to calibrate the stage. The upper limit of heating was at 600 °C, with a precision of the measurements ±1 °C during heating and ±0.2 °C during freezing. The software packages FLUIDS [47] and SoWat [48] were used for the estimation of the fluid compositions and properties. Densities were calculated from equations proposed by Driesner [49].

6. Results

6.1. Petrography

The latite shows a porphyritic, fine to medium grained (locally coarse grained, ~1 cm in size) texture and moderate to strong hydrothermal alteration (Figure 5a). It contains up to 40 vol % phenocrysts of quartz, K-feldspar, and minor plagioclase, and clinopyroxene, in a fine-grained ground mass dominated by quartz, K-feldspar, and sericite (Figure 5b,c). The main accessory minerals are magnetite, apatite, monazite, and zircon. The hydrothermal alteration assemblage includes biotite, K-feldspar, quartz, and minor titanite and magnetite related to potassic zone at depth; epidote, clinozoisite, chlorite, and albite related to propylitic zone; and sericite, quartz, pyrite, kaolinite, dolomite and rutile related to sericitic alteration. The surface of the latite bears a significant amount of totally oxidized metallic mineralization.

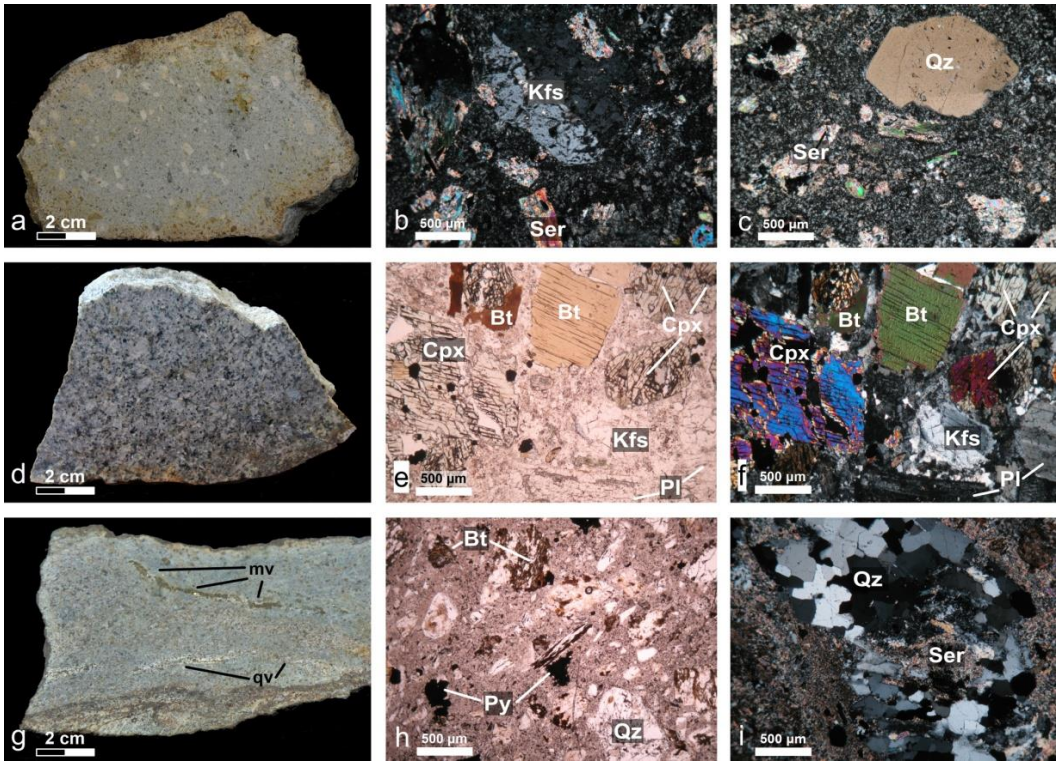

Figure 5. Hand specimens of rock samples and photomicrographs showing typical mineralogical paragenesis and alteration textures (plane polarized light: **e**, **h**; cross-polarized light: **b**, **c**, **f**, **i**) of the latite (**a**–**c**) and the quartz monzonite (**d**–**i**) from Vathi: (**a**) Fine-grained latite exhibiting a porphyritic texture with K-feldspar phenocrysts; (**b**) Magmatic K-feldspar (Kfs) altered to sericite (Ser) in a medium-grained ground mass composed of sericite and quartz; (**c**) Quartz (Qz) and sericite (Ser) in a fine-grained ground mass composed of sericite and quartz; (**d**) Equigranular quartz monzonite; (**e**,**f**) Magmatic clinopyroxene (Cpx), biotite (Bt) and K-feldspar (Kfs); (**g**) Mineralized veinlets (mv) comprising mainly pyrite and barren quartz veinlets (qv) crosscutting the quartz monzonite; (**h**) Magmatic biotite (Bt) and quartz (Qz) with disseminated pyrite (Py); (**i**) Quartz (Qz) vein with sericite (Ser) crosscutting the quartz monzonite.

The quartz monzonite is a micro- to equi-granular, locally porphyritic intrusion grey to light brown in color (Figure 5d). It consists of plagioclase, quartz, biotite, clinopyroxene, and hornblende, with accessory zircon and apatite crystals less than 2 mm in size (Figure 5e,f). The hydrothermal alteration assemblage in the quartz monzonite consists of biotite, K-feldspar, magnetite, titanite (potassic alteration), chlorite and sericite (sericitic alteration). Metallic minerals include pyrite and chalcopyrite. Mineralized and unmineralized quartz veinlets (up to 2 cm wide) crosscut the rock (Figure 5g).

The phreatic breccia consists of medium to strongly hydrothermally altered fragments of gneiss, schist, and latite of various sizes (up to 30 cm long) and shapes (Figure 6a,b). The breccia is extensively oxidized and well cemented by an argillaceous matrix. Towards the margins of the breccia body the fragments are more abundant, coarse, and angular in shape. The matrix is composed of illite, kaolinite, sericite, quartz, and oxidized metallic mineralization. Textural and mineralogical characteristics such as the heterolithic well-cemented fragments, their sizes and shapes, the fine argillaceous matrix, the oxidized mineralization, and the absence of cavities, classify this breccia as phreatic, according to the criteria of Sillitoe [50].

The cataclasite is composed of angular quartz fragments (up to 2 cm) and of a dark colored, fine-grained, silicified matrix (Figure 6c). Quartz is the main mineral while the hydrothermal alteration assemblage includes microcrystalline quartz and pyrophyllite.

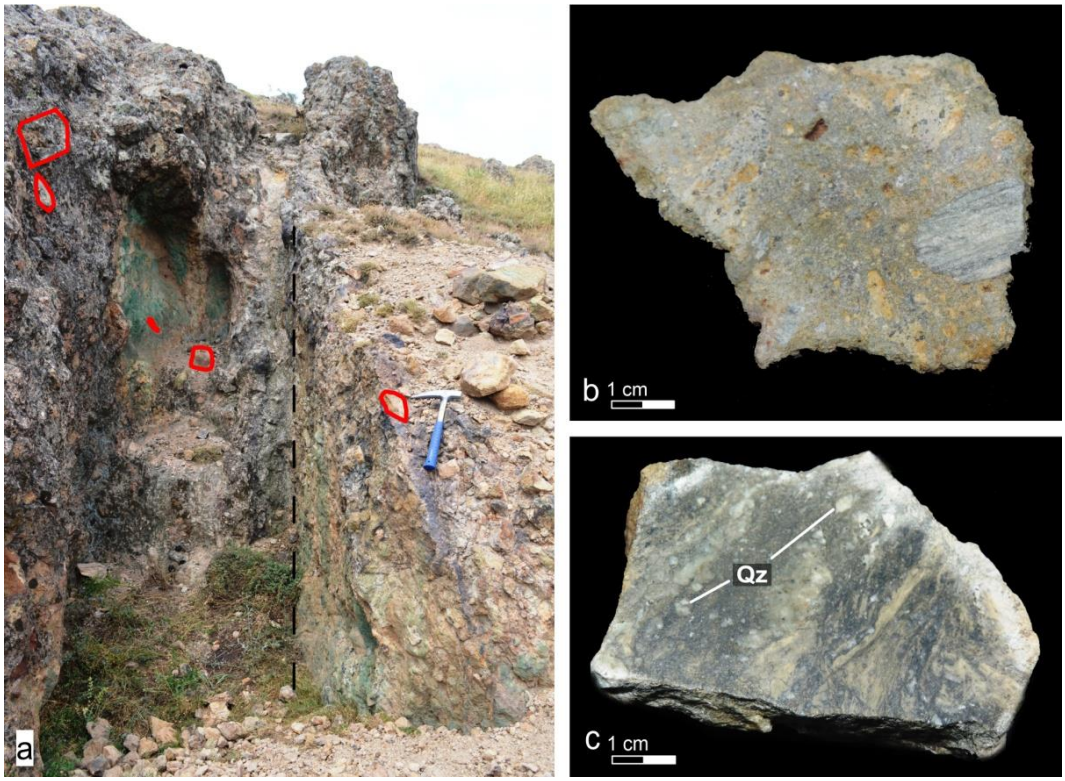

Figure 6. Phreatic breccia and cataclasite at Vathi: (**a**) Fragments of gneiss (highlighted in red boxes) of various sizes and shapes near the margins (dashed line) of the breccia; (**b**) Angular and sub-rounded fragments of gneiss and latite within a well-cemented argillaceous and oxidized matrix in a breccia sample; (**c**) Angular quartz (Qz) fragments within a dark colored, fine grained, silicified matrix in a cataclasite sample.

6.2. Lithogeochemistry

The compositions of 15 samples of latite, three samples of quartz monzonite, and single samples of supergene mineralization, phreatic breccia, and cataclasite are shown in Tables 1 and 2. Due to the localized but extensive hydrothermal alteration of the magmatic

rocks, the geochemical affinity and the classification were based on carefully selected fresh or least propylitized samples. Samples Vath 41 (quartz monzonite) and Vath 42 (latite; slightly propylitized), as well as unaltered quartz monzonite sample reported by Filippidis et al. [45] were evaluated (Figure 7a,b).

Samples Vath 41 and Vath 42 have similar silica contents of 63.05 wt % and 61.57 wt % SiO_2, respectively (Table 1). They have a high total alkali content, ranging from 6.55 to 8.70 wt % $K_2O + Na_2O$, and plot in the alkali-calcic to slightly alkali fields in Figure 7a. The two magmatic rock types are classified as quartz monzonite and as latite (Figure 7b).

The altered latite samples are characterized by wide variations in major-element composition (Table 1). Samples with SiO_2 content of about 70 wt % are associated with sericitic alteration. For significantly oxidized samples, the Fe_2O_3 content ranges from 10.35 to 20.13 wt %. Strontium and large ion lithophile element contents show significant variations in composition (Table 2), which is likely due to hydrothermal alteration and weathering intensity. Samples Vath 41 and Vath 42 contain 1269.1 and 1173.2 ppm Sr, respectively. In addition, high values are observed for Rb (Vath 41 165.3 ppm, Vath 42 120.1 ppm), and Ba (Vath 41 1513.8 ppm, Vath 42 867.8 ppm). These samples are also enriched in high field strength elements (HFSE; Zr, Hf, Nb, and Ta) (Table 2).

Chondrite-normalized rare earth elements (REEs) for the Vathi magmatic rocks show REE enrichment with a relatively flat heavy REE pattern (Table 2; Figure 8). The latite (Vath 42), quartz monzonite (Vath 41), and the phreatic breccia (Vath 15) possess ΣREE contents of 279.16, 370.46, and 1851.25 ppm, respectively. Quartz monzonite and latite samples appear 10 to 100 times more enriched in REEs compared to chondrite, whereas the phreatic breccia sample is significantly more enriched in LREEs, especially La (613.1 ppm) and Ce (894 ppm).

Table 1. Chemical compositions for major elements of analyzed samples from Vathi.

	Latite										Quartz Monzonite		Oxidized Mineralization	Cataclasite
	Propylitic Alteration		Sericitic Alteration								Sericitic Alteration	Relatively Fresh	Sericitic Alteration	
	Vath 10	Vath 42	Vath 1	VTH 3	VTH 4	VTH 11	VTH 12	VTH 14	Vath 17	Vath 27b	Vath 32	Vath 41	VTH 6	Vath 33
	wt %													
SiO_2	66.73	61.57	71.99	56.83	55.79	59.58	63.82	56.93	67.09	69.35	69.69	63.05	7.58	66.70
Al_2O_3	16.35	15.85	15.91	13.05	13.08	14.27	15.03	13.56	14.80	16.88	15.67	16.13	4.45	16.67
Fe_2O_3	3.38	5.68	2.67	19.22	20.95	10.98	5.65	0.69	8.26	2.40	3.14	5.09	73.31	3.34
CaO	0.26	2.63	0.05	0.05	0.09	0.29	0.13	0.09	0.03	0.16	0.05	3.13	0.07	1.11
MgO	0.32	2.82	0.53	0.29	0.50	0.28	0.27	0.25	0.59	0.51	0.50	1.78	0.17	1.85
Na_2O	0.36	4.38	0.14	0.07	0.10	0.70	0.42	0.25	0.09	0.15	0.15	4.01	bdl	3.06
K_2O	8.79	2.67	5.12	4.10	4.55	5.90	7.69	5.19	5.22	4.94	6.84	4.69	0.80	4.22
MnO	0.02	0.04	0.01	0.01	0.03	0.01	bdl	bdl	0.02	bdl	0.01	0.12	0.02	0.03
TiO_2	0.48	0.49	0.48	0.38	0.40	0.41	0.44	0.44	0.42	0.54	0.48	0.51	0.05	0.84
P_2O_5	0.35	0.25	0.08	0.33	0.27	0.53	0.22	0.06	0.12	0.07	0.05	0.31	0.73	0.13
Cr_2O_3	bdl	bdl	bdl	bdl	bdl	bdl	bdl	bdl	bdl	bdl	bdl	0.01	bdl	bdl
SrO	n.a.	0.13	n.a.	n.a.	n.a.	n.a.	n.a.	n.a.	n.a.	n.a.	n.a.	0.14	n.a.	n.a.
BaO	0.16	0.09	n.a.	n.a.	n.a.	n.a.	n.a.	n.a.	0.02	0.07	0.08	0.16	n.a.	0.17
LOI *	2.21	3.03	2.62	5.10	3.90	5.70	3.60	9.22	2.77	4.36	2.82	1.46	10.70	1.98
Total	99.41	99.63	99.60	99.43	99.66	98.65	97.27	86.68	99.43	99.43	99.48	100.59	97.88	100.10

* LOI = Loss of ignition, bdl = below detection limit, n.a. = not analyzed.

Table 2. Chemical compositions for trace elements and rare earth elements (REE) of analyzed samples from Vathi.

	Latite														Quartz monzonite			Ox. miner.*	Breccia *	Cataclasite
	Propylitic Alteration	Sericitic Alteration													Sericitic Alteration		Rel. Fresh *	Sericitic Alteration		
	Vath 10	Vath 19	Vath 42	Vath 1	VTH 3	VTH 4	Vath 5	Vath 7	VTH 11	VTH 12	Vath 12a	VTH 14	Vath 17	Vath 20	Vath 27b	Vath 30	Vath 32	Vath 41	VTH 6	Vath 15	Vath 33
Trace elements (ppm)																					
Mo	1.88	5.16	0.36	319.1	49.3	1.9	5.02	146.25	57.4	39.3	46.11	62.1	29.97	47.98	20.9	2.20	4.96	1.24	>2000	340.7	1.77
Cu	85.04	88.18	116.8	403.7	1449.8	1277.0	1273.5	1072.5	9297.0	>10000	340.98	>10000	1502.0	142.94	611.7	17.31	15.33	54.3	>10000	722.3	109.19
Pb	51.06	306.7	116.6	93.44	23.8	41.1	76.03	28.96	39.9	99.1	82.33	89.1	10.50	139.48	98.63	137.2	17.89	51.0	977.3	27.51	20.43
Zn	22.0	20.4	54.0	39.5	115.0	212.0	19.4	28.0	38.0	28.0	16.4	9.0	37.0	108.3	67.2	155.5	19.0	39.0	39.0	33.5	32.5
Ag	0.6	0.7	0.45	3.0	0.8	1.0	1.1	0.77	0.3	2.4	0.392	4.6	0.1	0.939	0.8	0.3	0.07	0.12	4.2	3.51	0.3
Ni	2.0	1.7	40.4	2.0	6.7	6.3	1.8	3.3	5.7	2.3	2.6	1.2	4.2	9.1	5.6	91.9	3.9	4.9	46.7	3.7	41.4
Co	0.9	0.7	38.4	0.9	1.6	2.5	0.5	1.0	3.4	0.6	1.0	1.1	3.3	2.8	2.5	103.3	1.9	23.4	41.7	1.0	6.8
Mn	75.0	58.0	232.0	90.0	n.a.	n.a.	96.0	70.0	n.a.	n.a.	68	n.a.	191.0	46.0	49.0	6798.0	93.0	427.0	n.a.	61.0	165
As	2.7	4.0	30.2	5.4	2.9	2.4	7.8	3.7	2.4	1.4	3.0	8.4	3.3	182.8	2.3	132.3	4.8	3.6	472.6	61.1	4.8
U	9.6	9.8	8.31	9.4	71.3	14.0	32.1	27.6	20.4	32.4	11.7	14.3	11.8	10.5	11.2	14.9	21.4	16.3	262.6	40.5	2.7
Th	45.5	44.4	44.4	37.4	37.0	37.2	42.0	43.2	38.9	40.4	20.7	39.7	37.3	52.6	41.3	34.4	55.1	67.8	75.2	36.2	13.0
Sr	196.0	208.0	55.4	28.0	61.8	10.7	11.0	200.0	290.7	268.9	237.0	320.8	10.0	233.0	150.0	131.0	128.0	57.7	64.4	47.0	187.0
Cd	0.06	0.02	0.27	bdl	0.8	7.7	0.68	0.18	2.4	2.5	bdl	bdl	bdl	bdl	0.21	0.15	bdl	0.09	6.9	bdl	0.03
Sb	3.76	2.93	1.82	5.37	0.1	0.3	6.58	3.42	0.2	0.1	1.65	0.2	3.51	19.14	2.37	1.09	1.65	2.5	18.7	11.20	0.52
Bi	12.04	2.93	4.58	6.76	4.5	239.4	12.56	12.22	3.0	8.0	5.54	1.2	8.99	9.28	4.61	2.43	2.68	0.49	5.8	18.32	0.41
V	82.0	85.0	90.0	52.0	91.0	72	68.0	102.0	42.0	46.0	66.0	62.0	72.0	56.0	101.0	81.0	64.0	112.0	bdl	205.0	148.0
Cr	4.0	4.0	79.0	4.0	n.a.	n.a.	5.0	6.0	n.a.	n.a.	5.0	n.a.	4.0	5.0	5.0	7.0	5.0	81.0	n.a.	18.0	69.0
Ba	1219.0	1330.0	189.0	159	341.0	99.0	89.0	719.0	1266.0	1876	927.0	5043	78.0	158.0	478.0	59.0	208.0	144.0	74.0	176.0	1645.0
W	8.2	23.1	117.0	11.5	10.6	123.6	24.1	14.1	6.2	8.9	118.5	4.7	10.4	>200.0	7.7	72.6	12.1	181.4	13.9	43.6	6.4
Zr	63.5	64.7	184.0	52.8	176.3	162.4	51.6	65.0	175.5	192.0	57.5	192.6	44.7	58.8	53.5	52.1	58.7	6.2	25.5	38.2	1.1
Sn	7.3	7.6	4.2	15.4	8.0	32.0	16.3	10.3	9.0	5.0	4.3	5.0	8.3	10.7	12.7	8.4	2.0	1.8	3.0	8.3	3.6
Be	3.0	4.0	0.57	5.0	3.0	1.0	4.0	4.0	1.0	5.0	4.0	bdl	5.0	5.0	5.0	5.0	4.0	1.07	2.0	3.0	2.0
Sc	4.8	6.7	7.6	4.3	9.0	9.0	7.0	6.1	6.0	7.0	4.6	7.0	5.2	4.9	6.2	6.1	6.4	2.2	7.0	10.0	16.8
Y	15.0	15.7	27.1	9.5	19.5	53.9	12.5	14.9	31.1	35.7	11.2	16.3	7.5	9.9	13.8	20.8	6.7	15.1	28.5	27.0	22.3
Hf	2.47	2.54	0.16	2.01	4.6	4.3	2.07	2.69	5.0	4.9	2.43	5.7	1.78	2.35	2.12	2.21	2.39	0.3	0.8	1.46	0.02
Li	11.4	13.9	11.3	9.6	n.a.	n.a.	6.5	11.8	n.a.	n.a.	11.5	n.a.	10.4	16.8	23.9	7.2	10.5	4.8	n.a.	17.2	12.8
Rb	287.2	261.4	63.8	420.4	241.1	339.1	406.2	344.9	169.9	267.2	292.0	189.9	367.3	244.0	213.3	317.9	89.2	31.4	63.4	321.4	159.2
Ta	0.9	1.0	1.4	0.6	0.8	0.8	0.7	0.9	0.9	0.9	0.7	1.6	0.5	0,7	1.0	0.8	0.3	1.8	0.1	0.3	0.5
Nb	11.31	12.98	0.65	9.45	9.7	15.9	11.16	9.70	11.5	11.2	8.79	14.7	5.85	8,12	13.06	10.08	4.67	1.23	0.2	3.75	5.70
Cs	8.1	7.0	4.7	8.6	7.9	5.4	6.7	6.4	10.8	7.7	5.6	7.8	5.6	6,9	10.0	6.4	7.6	2.88	3.0	13.1	6.3
Ga	19.70	19.81	9.4	21.87	14.9	15.2	23.50	21.00	15.9	15.0	20.59	15.2	19.70	18.92	21.29	18.77	18.83	5.97	5.8	23.08	24.34
In	0.19	0.14	0.006	0.20	n.a.	n.a.	0.56	0.33	n.a.	n.a.	0.42	n.a.	0.63	0.29	0.21	0.19	0.49	0.014	n.a.	0.81	0.04
Se	0.5	1.4	1.2	0.6	0.7	bdl	0.6	bdl	10.5	0.5	3.9	8.3	0.5	4,9	bdl	0.4	2.3	1.2	47.4	bdl	bdl
Te	bdl	0.10	0.49	0.09	bdl	bdl	bdl	0.09	bdl	bdl	0.27	bdl	0.05	0.51	bdl	0.49	0.17	0.49	3.0	0.09	0.09
Tl	5.72	4.64	0.83	5.44	0.9	0.9	4.30	4.61	0.6	0.8	4.45	0.6	4.19	3.50	4.12	4.41	5.23	0.21	0.3	4.34	2.38
Hg	n.a.	n.a.	0.2	n.a.	0.01	bdl	n.a.	n.a.	0.01	bdl	n.a.	0.11	n.a.	n.a.	n.a.	n.a.	n.a.	0.19	0.86	n.a.	n.a.
V/Sc	17.08	12.69	11.84	12.09	10.11	8.00	9.71	16.72	7.00	6.57	14.35	8.86	13.85	11.43	16.29	13.28	10.0	50.91	n.a.	20.50	8.81
Trace elements (ppb)																					
Re	bdl	3.0	3.0	bdl	n.a.	n.a.	bdl	bdl	n.a.	n.a.	3.0	n.a.	bdl	5.0	bdl	bdl	bdl	3.0	n.a.	3.0	bdl
Au	8.0	6.0	36.3	20.0	103.0	1170.0	118.2	7.2	135.0	98.0	20.7	26.0	30.0	32.6	4.0	20.0	4.0	37.0	6996.0	724.0	7.0

Table 2. *Cont.*

	Latite															Quartz monzonite			Ox. miner.*	Breccia *	Catacla-Site
	Propylitic Alteration	Sericitic Alteration														Sericitic Alteration		Rel. Fresh *	Sericitic Alteration		
	Vath 10	Vath 19	Vath 42	Vath 1	VTH 3	VTH 4	Vath 5	Vath 7	VTH 11	VTH 12	Vath 12a	VTH 14	Vath 17	Vath 20	Vath 27b	Vath 30	Vath 32	Vath 41	VTH 6	Vath 15	Vath 33
	Rare earth elements (ppm)																				
La	59.3	35.2	68.2	5.5	31.4	45.6	32.1	73.9	54.3	53.4	37.9	42.7	65.2	97.7	35.7	68.0	32.8	82.8	22.8	613.1	33.8
Ce	107.0	77.68	122.70	12.9	75.1	139.1	91.48	140.60	101.0	119.0	73.74	94.4	122	160.02	75.8	144.5	63.73	152.9	39.6	894.0	69.13
Pr	12.7	8.7	13.02	1.7	9.11	20.26	12.7	15.1	10.6	12.8	8.2	11.0	13.5	16.4	9.1	17.6	7.4	16.02	3.69	79.1	8.8
Nd	38.8	30.3	46.2	8.4	37.3	93.1	44.2	48.9	40.6	45.9	30.3	38.6	45.9	45.7	31.5	61.2	26.4	85	13.9	211.1	32.9
Sm	6.2	5.0	8.14	2.2	6.00	17.4	8.7	8.1	7.51	8.73	5.2	6.92	6.5	6.3	4.9	10.9	4.5	10.2	2.93	23.4	6.2
Eu	1.7	1.2	1.63	0.5	1.38	3.59	2.4	2.2	1.99	1.96	1.0	1.24	1.9	1.8	1.1	2.3	1.0	2.42	0.95	5.1	1.1
Gd	4.1	4.3	6.59	2.0	4.38	13.67	6.0	5.5	6.46	7.43	3.6	4.98	3.8	4.1	4.0	7.2	2.9	7.84	3.86	12.7	5.7
Tb	0.4	0.5	0.84	0.2	0.60	1.96	0.6	0.6	1.00	1.09	0.3	0.69	0.3	0.3	0.4	0.8	0.1	1.02	0.80	1.3	0.6
Dy	3.2	3.2	4.41	2.1	3.44	10.43	3.5	3.7	5.82	6.39	1.9	3.41	1.9	2.2	2.6	4.1	1.3	4.8	5.35	5.5	3.8
Ho	0.6	0.7	0.95	0.4	0.60	1.90	0.6	0.7	1.19	1.35	0.4	0.6	0.4	0.4	0.6	0.8	0.3	0.98	1.14	0.9	0.8
Er	1.8	1.8	2.90	1.0	2.06	5.09	1.8	2.0	3.77	3.86	1.3	1.69	0.9	1.0	1.8	1.8	0.7	2.84	3.10	2.1	1.8
Tm	0.3	0.3	0.39	0.2	0.33	0.77	0.3	0.3	0.54	0.59	0.2	0.27	0.2	0.2	0.3	0.3	0.1	0.44	0.52	0.4	0.3
Yb	1.9	1.8	2.76	1.2	2.11	3.83	1.8	2.0	3.51	3.87	1.2	1.69	1.4	1.5	1.8	1.7	0.9	2.76	3.29	2.2	1.6
Lu	0.3	0.2	0.43	0.2	0.35	0.61	0.3	0.3	0.51	0.60	0.2	0.29	0.2	0.2	0.3	0.3	0.2	0.44	0.45	0.3	0.2
ΣREE	238.1	170.9	279.16	38.5	174.16	357.31	206.5	303.9	238.41	267.38	165.4	208.47	263.7	337.8	169.88	321.55	142.33	370.46	102.38	1851.25	166.73

* Rel. fresh = relatively fresh, Ox. miner. = oxidized mineralization, Breccia = phreatic breccia, bdl = below detection limit, n.a. = not analyzed.

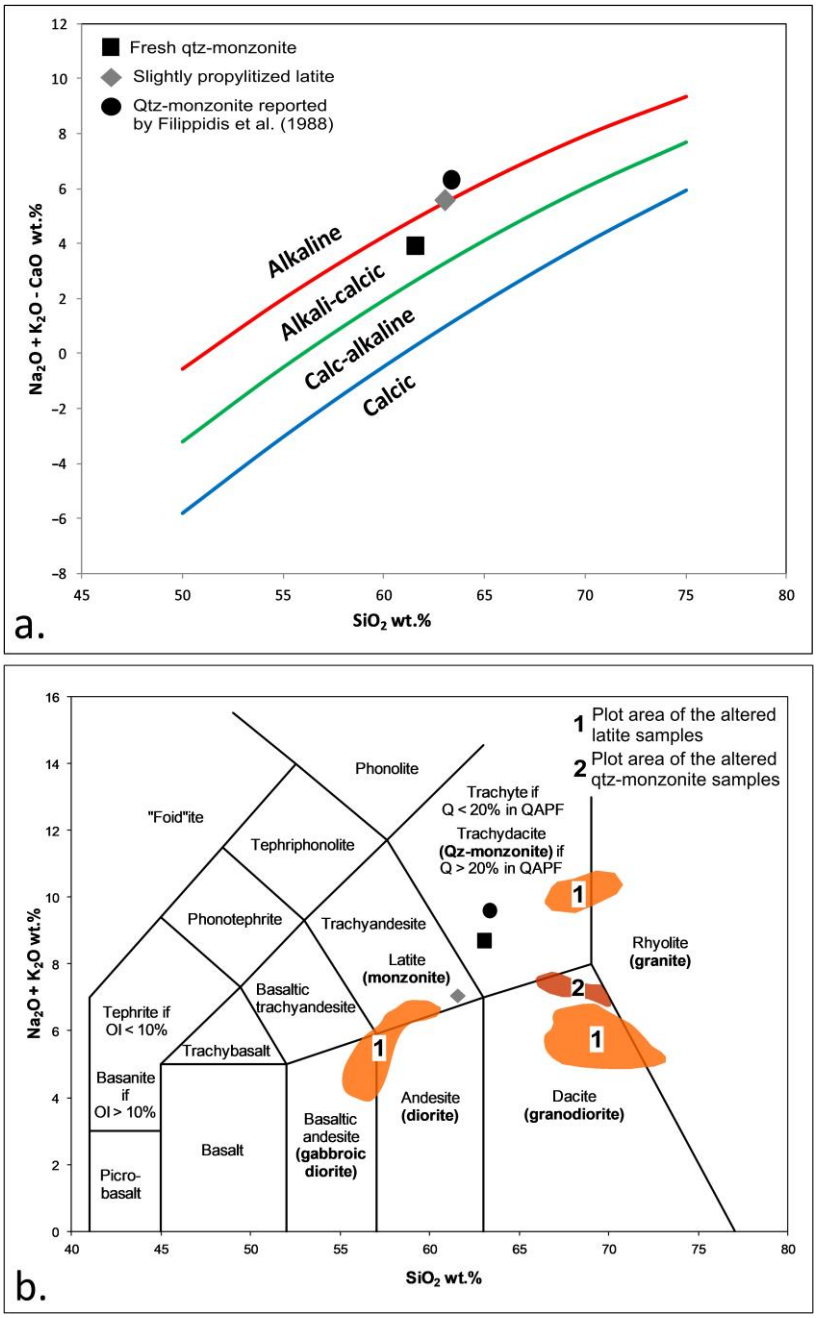

Figure 7. (**a**) Plot of alkalis + CaO versus silica for magmatic rocks from Vathi. They are characterized by alkali-calcic to Scheme 51. (**b**) Plot of total alkalis (wt %) vs. SiO_2 (wt %) (after [51–53]).

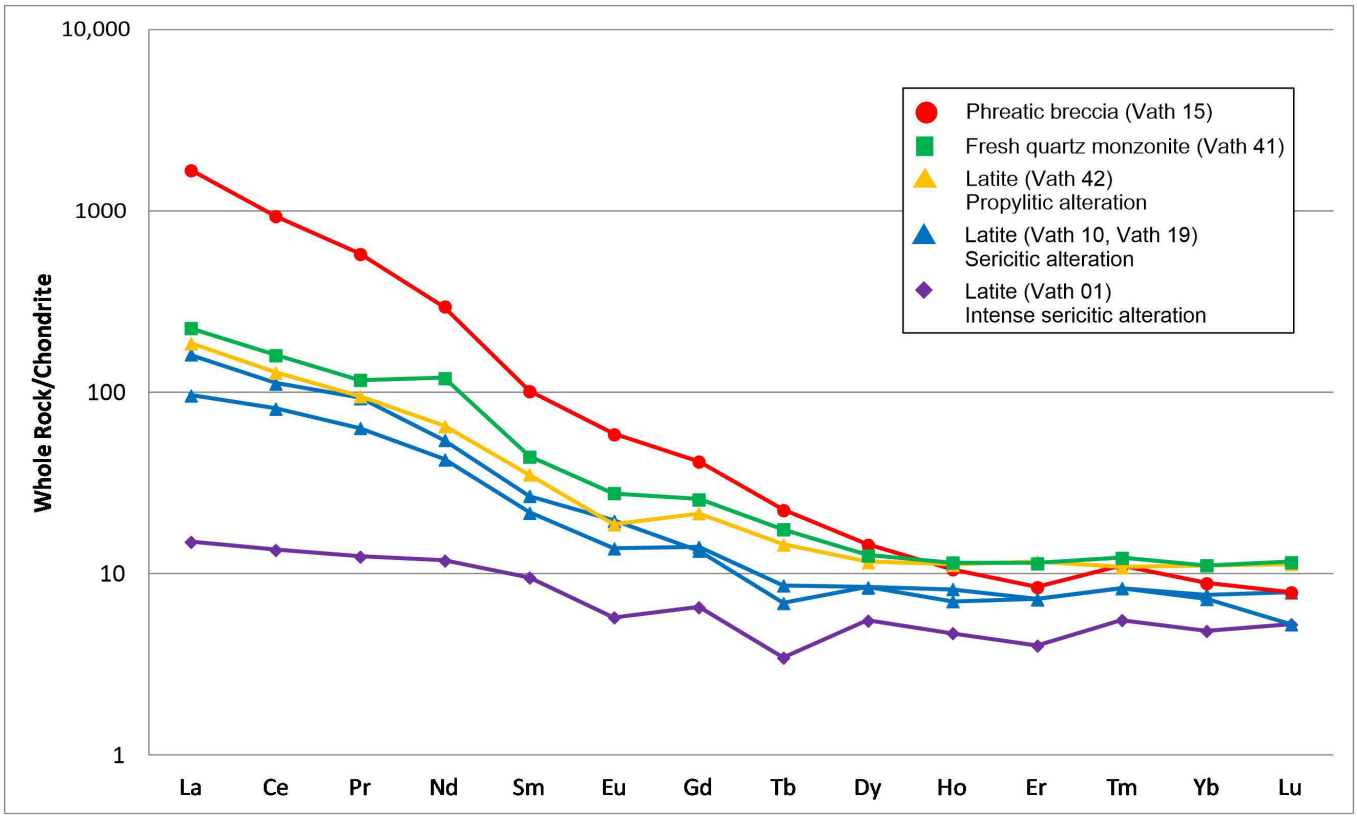

Figure 8. Chondrite normalized REE discrimination diagram for the Vathi magmatic rocks (chondrite normalized values after Taylor and McLennan; [54]).

6.3. Hydrothermal Alteration

Three main types of hydrothermal alteration affected the magmatic and adjacent metamorphic rocks: potassic, propylitic, and sericitic (Figure 9). No particular patterns are ascribed to the distribution of the hydrothermal alteration, which is mostly spatially associated with the quartz monzonite and regional structures.

Potassic alteration, spatially and temporally related to the quartz monzonite, is generally restricted in space due to the subsequent sericitic alteration overprint. Drill core samples show that it mainly occurs at depth but it is also weakly exposed at the surface [45] (Figure 9). It was previously described by Frei [16] and Filippidis et al. [45] who recognized biotite-K-feldspar-pyrite veinlets in the drill core from the quartz monzonite stock, which is located 2 km north of Ragian 1 Hill (Figure 3; inset map). These veinlets are approximately 1 cm wide and consist of biotite, K-feldspar, magnetite, titanite, and quartz (Figure 10a). Fine-grained hydrothermal biotite was also found in A-type veinlets and disseminated in the groundmass of quartz monzonite.

The propylitic alteration is generally weak and affects both the quartz monzonite and the latite (Figure 9). The characteristic hydrothermal minerals, also reported by Frei [16], are epidote, clinozoisite, chlorite, minor sericite, pyrite, and traces of albite (Figure 10b).

The sericitic alteration affects both the magmatic and metamorphic rocks, and the phreatic breccia (Figure 9). In the latite, it overprints the propylitic alteration and locally results in the complete replacement of feldspar, especially at the eastern part of the porphyry system. In addition, sericite, pyrite, quartz, kaolinite, dolomite, and rutile are also present in the altered latite (Figure 10c). Sericite forms acicular to prismatic aggregates, which are accompanied by disseminations and masses of hematite. The K-feldspar replacement by sericite is generally controlled by the distribution of micro-fractures. In these cases, only the relic crystal habit of K-feldspar remains, forming vugs of different sizes. An epithermal overprint occurs locally within the sericitic alteration and is manifested as veinlets and as

euhedral crystals (<30 μm in size) of hydrothermal quartz with fine-grained pyrophyllite in the groundmass of the latite. This epithermal event is mainly traced along an E-W trending structure on the northern side of Ragian 1 Hill into a latite cataclasite, which includes angular quartz fragments and pyrophyllite in a silicified groundmass (Figure 10d).

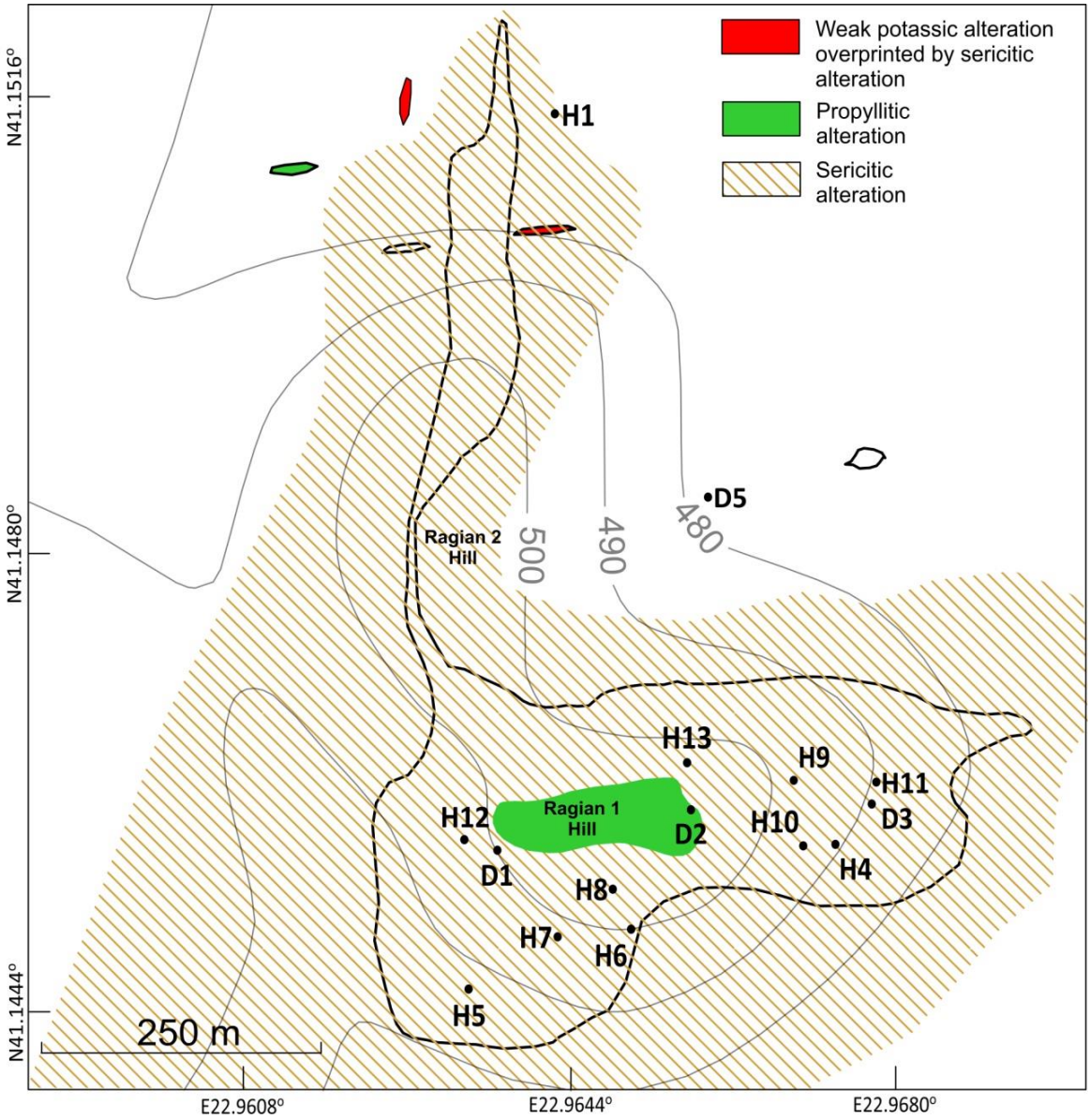

Figure 9. Spatial distribution of the hydrothermal alterations of the Vathi porphyry system. The locations of the drill holes are also shown (advice Figure 3).

6.4. Ore Mineralization

Ore mineralization at the Vathi porphyry system is hosted by quartz monzonite, latite, phreatic breccia, and surrounding metamorphic rocks. At the surface, the metallic mineralization is almost totally oxidized. The oxidation zone has a maximum depth of 90 to 100 m and is associated with a narrow secondary enrichment zone, 2 m deep [46] (Figure 3c). The hypogene mineralization at the surface is restricted to the quartz monzonite, and in the drill core samples, it is well exposed below the secondary enrichment zone to an unknown depth.

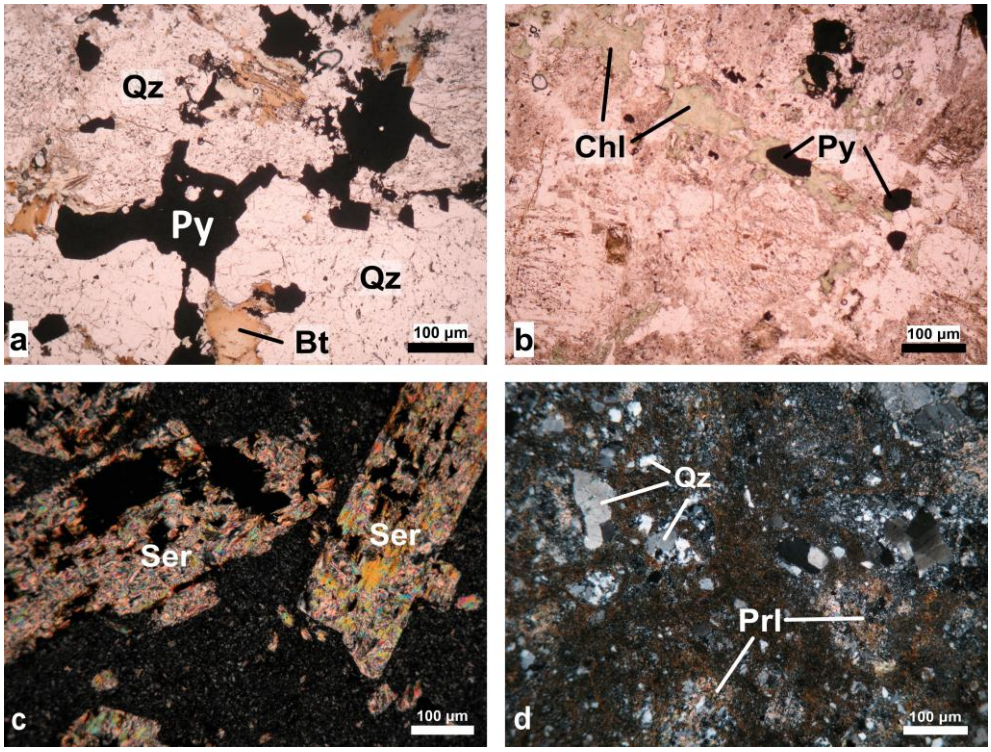

Figure 10. Photomicrographs of textures and minerals of the hydrothermal alterations (plane polarized light: a, b; cross-polarized light: c, d): (**a**) Hydrothermal biotite (Bt), quartz (Qz), and pyrite (Py) from an A-type veinlet of the potassic alteration in a quartz monzonite drill core sample; (**b**) Hydrothermal chlorite (Chl) and pyrite (Py) of the propylitic alteration in the quartz monzonite; (**c**) Sericite (Ser) in altered K-feldspar of the sericitic alteration in latite; (**d**) Clusters and disseminations of quartz (Qz) and pyrophyllite (Prl) replaced by iron oxides in the groundmass of cataclasite.

6.4.1. Hypogene Mineralization

The mineralization forms disseminations, aggregates, veins, and veinlets. Four assemblages are present: (1) pyrite + chalcopyrite + bornite + molybdenite + magnetite associated with potassic alteration, (2) pyrite + chalcopyrite related to propylitic alteration, (3) pyrite + chalcopyrite + native gold ± tetradymite associated with sericitic alteration, and (4) sphalerite + galena + arsenopyrite + pyrrhotite + pyrite ± stibnite ± tennantite related to the epithermal overprint (Figure 11). Furthermore, four early to late-stage hydrothermal vein types correspond to M-, A-, D-, and epithermal (E-type) veins, as described by for example, Hedenquist et al. [55] and Sillitoe [56].

The mineralization associated with the potassic alteration occurs in quartz monzonite and is present mainly along drill hole D1 (66-75 m interval) [46]. It forms A- and M-type veins and disseminations, and it consists mostly of pyrite and chalcopyrite with minor molybdenite, bornite, and magnetite. A-type quartz veins (up to 2 cm wide) are rare but were observed in the drill core samples (Figure 12a). The M-type veins, found on the surface and at the depth, contain magnetite with quartz and titanite (Figure 12b). At a depth of 140 m, pyrite and chalcopyrite are present in approximately equal amounts, whereas at 166 m, only chalcopyrite and molybdenite occur. Restricted amounts of pyrite and chalcopyrite were observed in the propylitic alteration that extends in both magmatic rock types at the surface and at a depth of 40 to 140 m.

Pyrite and chalcopyrite, as well as minor amounts of rutile and ilmenite, occur in sericitic alteration mainly in latite but also in the phreatic breccia and surrounding metamorphic rocks [46]. The mineralization forms disseminations, aggregates, and D-type veins and veinlets and associated halos along cracks in the latite rock mass (Figure 12c). In some cases, D-type sheeted veins trending E-W form a dense system crosscutting the latite

(Figure 6). They are usually less than 1 cm wide, locally reaching up to 5 cm in width.A subsequent epithermal overprint is documented locally within the potassic and sericitic alteration. It mainly occurs as E-type veins at depth and consists of sphalerite, galena, arsenopyrite, pyrrhotite, and traces of tennantite, stibnite, rutile, and ilmenite.

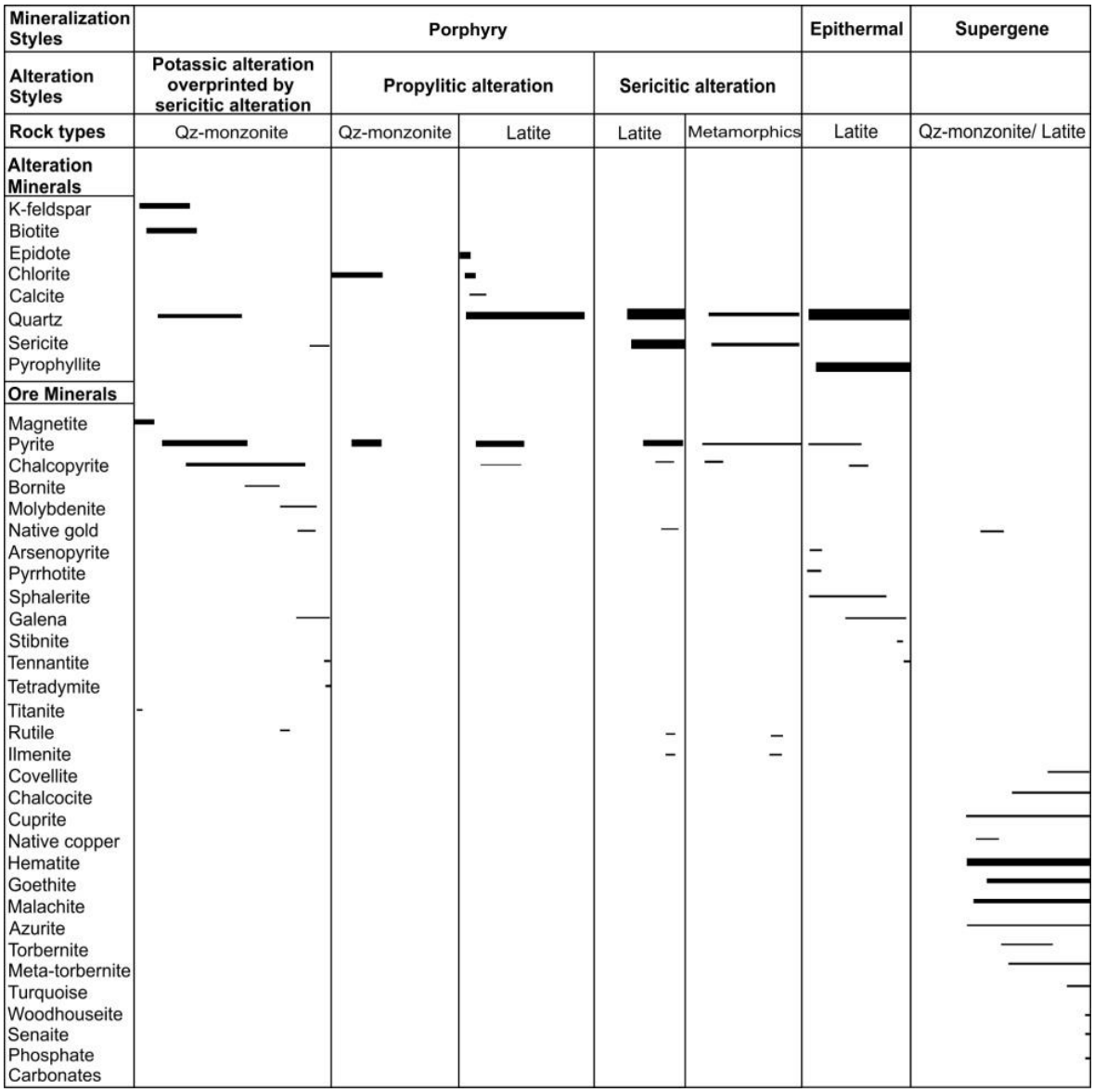

Figure 11. Ore and alteration minerals corresponding to each alteration zone in the Vathi porphyry Cu-Au±(Mo) deposit. Line thickness depicts the relative abundances of the minerals. Qz: quartz.

Pyrite is the most common sulfide in the Vathi porphyry system, and it is intergrown with chalcopyrite, bornite, pyrrhotite, sphalerite, and galena. Locally, it hosts rounded inclusions of chalcopyrite, as well as euhedral inclusions of magnetite and molybdenite. It occurs as disseminations or intergrowths of anhedral to euhedral grains, with sizes varying from 25 to 200 μm and from 400 μm to 2 cm, respectively (Figure 13a). Pyrite also forms veinlets (up to 3 mm in size) and minor dispersions, in which galena locally appears in the interstices (Figure 13b).

Chalcopyrite is the second most abundant sulfide and is found mainly in the potassic alteration where it is intergrown with pyrite, magnetite, molybdenite, and bornite (Figure 13c–f). It occurs as disseminated grains (<200 μm in size), irregular aggregates (<300 μm in size), and rounded inclusions (<20 μm in diameter) in pyrite. Chalcopyrite

also forms thin veinlets (<0.5 cm in width) along with pyrite inclusions (10–20 μm in size). Below a depth of 166 m, mineralized stockworks with chalcopyrite and molybdenite are present (Figure 13e).

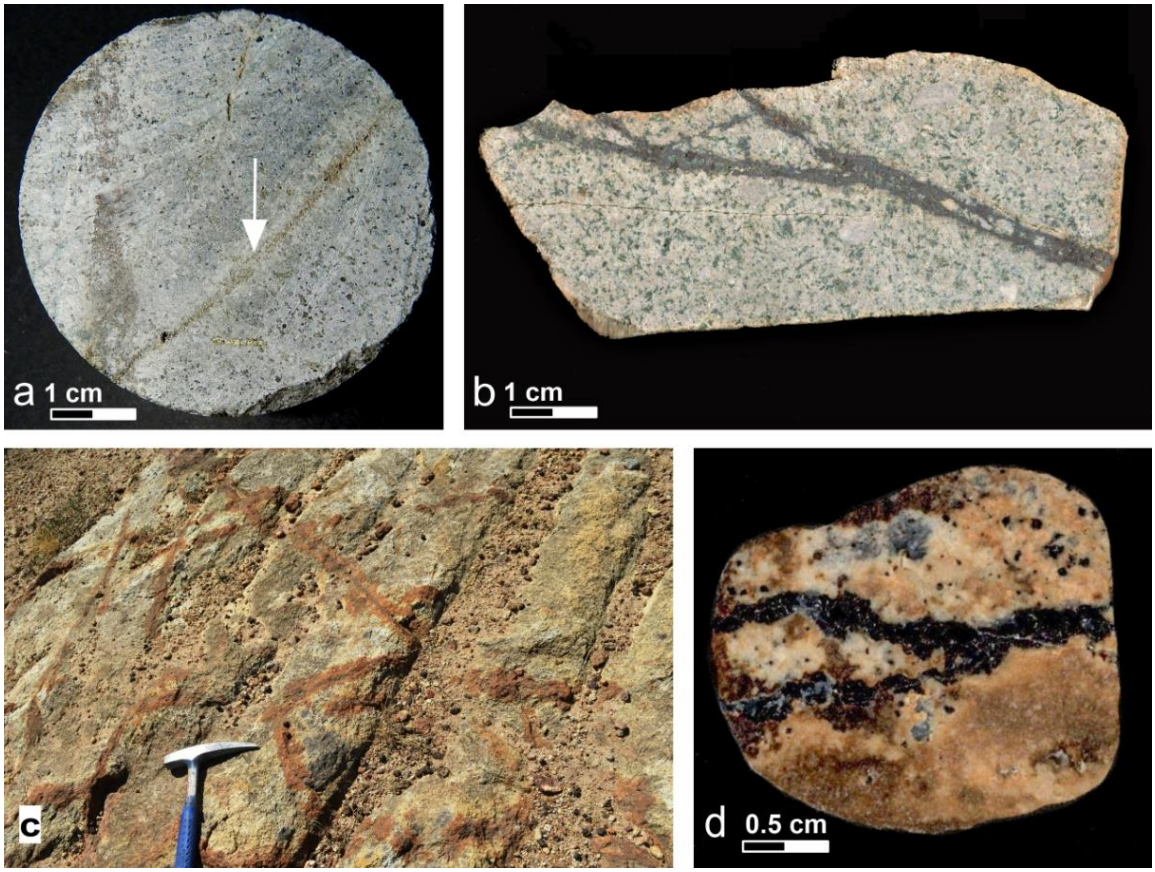

Figure 12. Photographs of textures and minerals in the Vathi porphyry system: (**a**) A-type veinlet from a drill core sample of the quartz monzonite containing pyrite, chalcopyrite, and magnetite in the potassic alteration; (**b**) Surface M-type veinlet with magnetite crosscutting the quartz monzonite from a stock NW of Ragian 1 Hill; (**c**) D-type veins, 1 to 5 cm wide, crosscut the latite and contain oxidized pyrite, quartz, and sericite; (**d**) E-type veinlet with sphalerite and galena from a drill core sample of the latite.

Magnetite is associated with the potassic alteration forming M-type veinlets (up to 1 cm wide) crosscutting the quartz monzonite (Figure 12b). It also occurs as disseminated crystals or intergrowths with chalcopyrite. In latite, massive magnetite is intergrown with pyrite, chalcopyrite, and minor titanite (Figure 13d). It is also found in chalcopyrite as subhedral to euhedral inclusions (Figure 13e).

Molybdenite occurs with pyrite and chalcopyrite in potassic alteration as small (<30 μm in length), disseminated, lamellar grains in latite (Figure 13e). In some cases, molybdenite also occurs as disseminations intergrown with prismatic rutile. Bornite in potassic alteration locally forms rounded inclusions, ranging between 15 and 100 μm in size in pyrite and chalcopyrite (Figure 13f).

Pyrrhotite is present at a depth below 166 m in E-type veins and is intergrown with pyrite and chalcopyrite (1 cm wide) (Figure 14a). Galena occurs in sericitic alteration and is intergrown with pyrite, chalcopyrite (<50 μm in width), and sphalerite. It appears in the interstices in pyrite veinlets and disseminations in quartz monzonite (Figure 13b), or it forms E-type veins (1 to 3 mm wide) with sphalerite and quartz (Figure 14b,c).

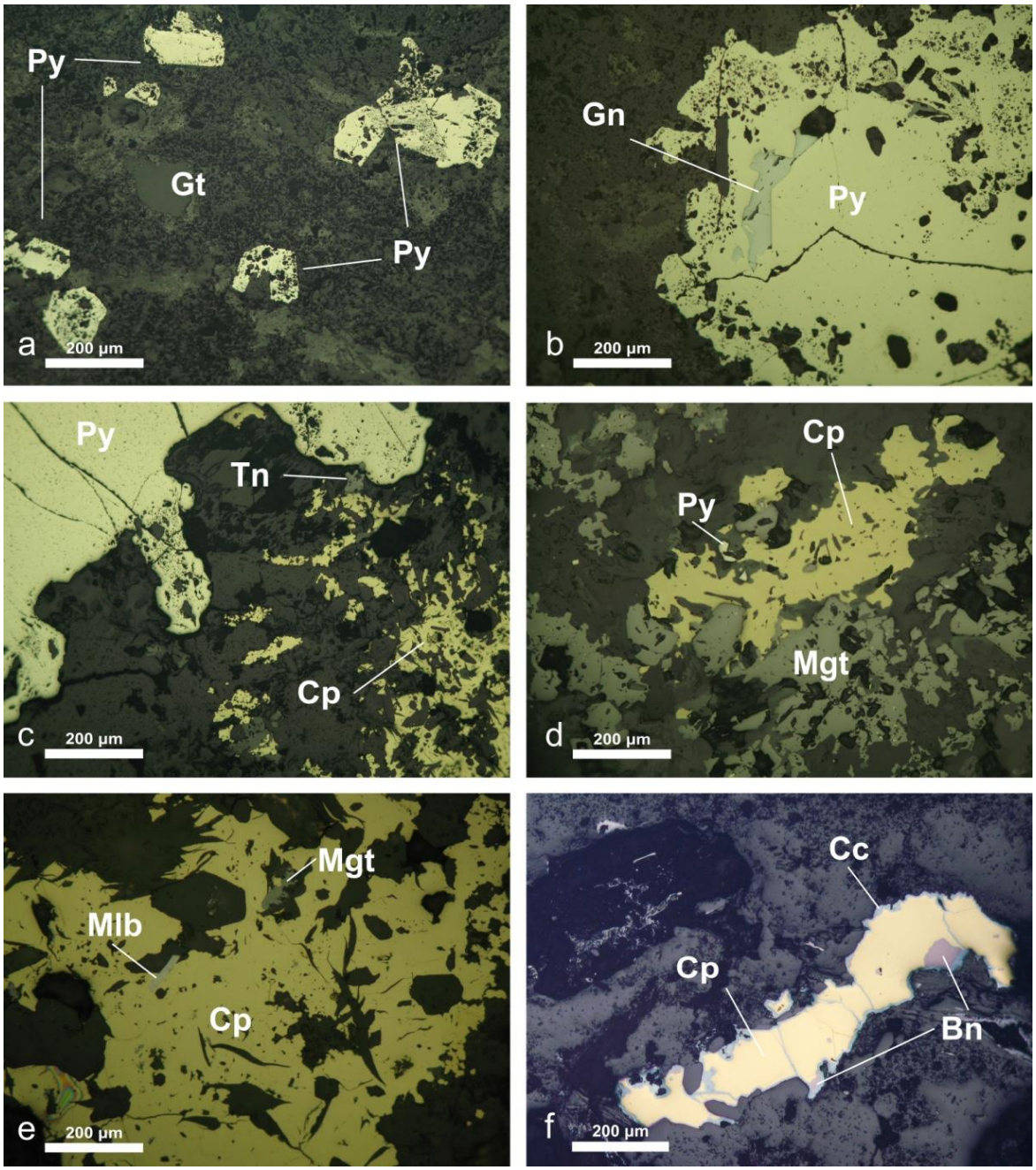

Figure 13. Photomicrographs of the hypogene mineralization in quartz monzonite (**a**,**b**) and latite (**c**–**f**) (plane reflected light: **a**–**f**: (**a**) Disseminated euhedral pyrite (Py) and goethite (Gt); (**b**) Galena (Gn) filling interstices in pyrite (Py); (**c**) Corroded pyrite (Py) and chalcopyrite (Cp) with minor tennantite (Tn); (**d**) Magnetite (Mgt) intergrown with chalcopyrite (Cp) and pyrite (Py); (**e**) Magnetite (Mgt) in chalcopyrite (Cp) and molybdenite (Mlb); (**f**) Chalcopyrite (Cp) and bornite (Bn) replaced by chalcocite (Cc).

Sphalerite, similar to galena, occurs as large anhedral grains intergrown with pyrite and chalcopyrite in sericitic alteration. In E-type veins, sphalerite contains numerous chalcopyrite inclusions (so-called chalcopyrite disease) and is intergrown with chalcopyrite, galena, arsenopyrite, minor pyrite, and quartz (Figure 14b,c). Arsenopyrite was observed only in the E-type veins along with sphalerite and galena. It mainly forms prismatic and rhombohedral crystals, <500 µm in length (Figure 14d), and it occurs in micro-cavities in latite along with quartz and pyrite.

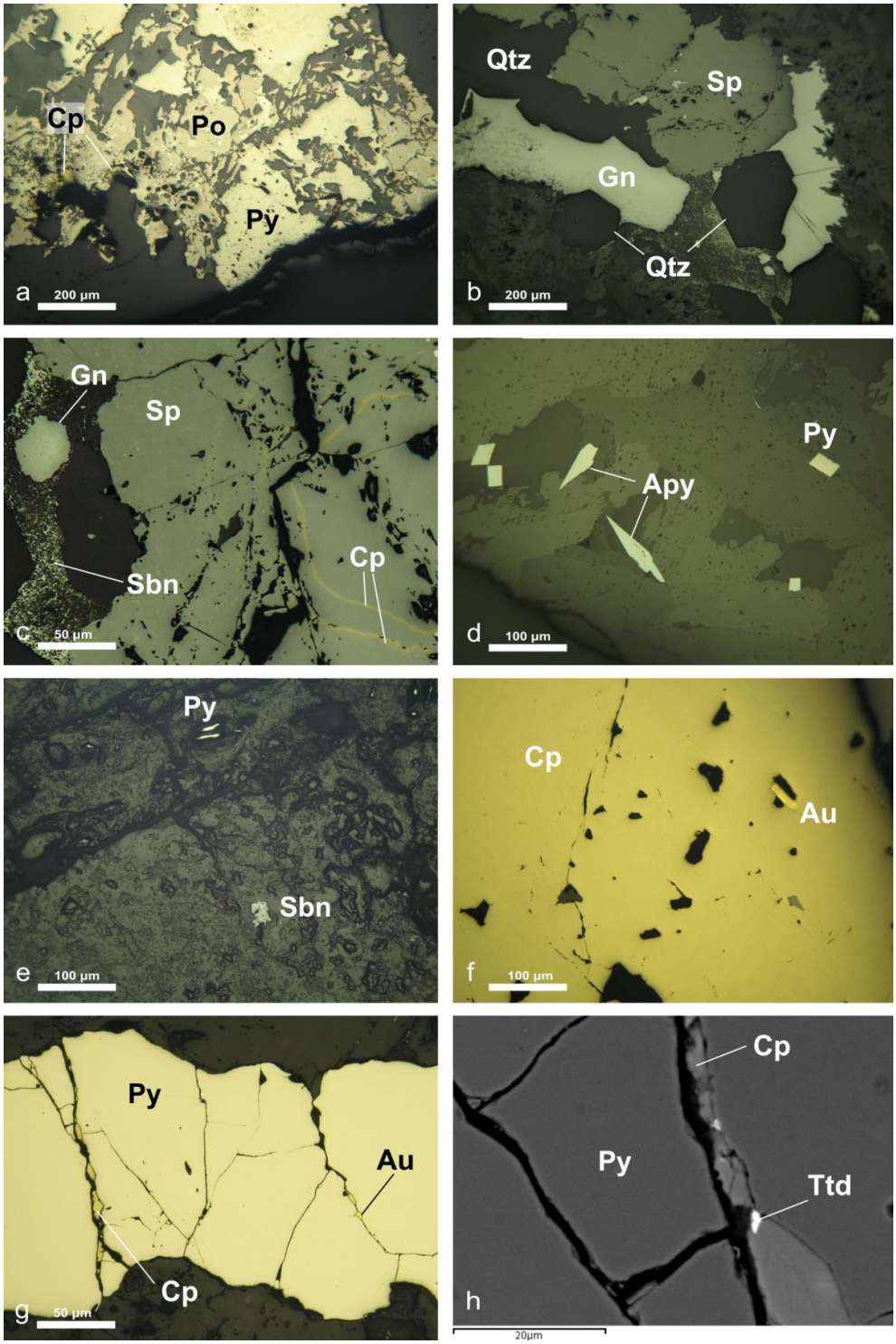

Figure 14. Photomicrographs of the hypogene mineralization in latite (**a**–**e**) and quartz monzonite (**f**,**g**) (plane reflected light: **a**–**g**), and an SEM back-scattered electron image (**h**) of a pyrite veinlet in the quartz monzonite: (**a**) Pyrrhotite (Po) is intergrown with pyrite (Py) and chalcopyrite (Cp) in an E-type epithermal vein; (**b**) Sphalerite (Sp), galena (Gn), and quartz (Qtz) in an E-type epithermal vein; (**c**) Sphalerite (Sp), galena (Gn), and stibnite (Sbn) inclusions of chalcopyrite (Cp) in an E-type epithermal vein; (**d**) Euhedral arsenopyrite (Apy) and pyrite (Py) in micro-cavities in the latite; (**e**) Stibnite (Sbn) and pyrite (Py) relicts in goethite; (**f**) Chalcopyrite (Cp) with an inclusion of native gold (Au); (**g**) D-type pyrite (Py) veinlet with chalcopyrite (Cp) and native gold (Au) in micro-cracks; (**h**) Chalcopyrite (Cp) and tetradymite (Ttd) filling micro-cracks in pyrite (Py).

Stibnite is present in traces (<50 μm in size) in sericitic alteration in latite (Figure 14e). Additionally, stibnite occurs in the E-type veins as tiny radiating and elongated crystals in cavities or as intergrowths with sphalerite and galena (Figure 14c). Tennantite is spatially related to sphalerite and galena in sericitic alteration, where it appears as tiny inclusions in sphalerite with galena and chalcopyrite as well as overgrowths on pyrite, chalcopyrite, and bornite (Figure 13c). Native gold occurs as inclusions 10 to 50 μm in size in pyrite and chalcopyrite and as infills between grains in pyrite veinlets related to sericitic alteration (Figure 14f). It is also found in goethite. In D-type pyrite veinlets, native gold (up to 20 μm in length) appears as infills along with chalcopyrite and tetradymite (Figure 14g). Veinlets of gold in goethite were reported previously by Markoulis (1970).

Tetradymite is a minor mineral up to 7 μm in size along with chalcopyrite and native Au in D-type pyrite veins in quartz monzonite where potassic alteration is overprinted by sericitic alteration (Figure 14h). Rutile occurs as prismatic crystals up to 50 μm in size in pyrite, chalcopyrite, and molybdenite in potassic and sericitic alterations. Ilmenite forms lamellar exsolutions in magnetite in the potassic alteration zone. It is also present in pyrite and chalcopyrite as euhedral crystals 20 to 40 μm in length.

6.4.2. Supergene Mineralization

The oxidation zone in latite contains masses, encrustations, and impregnations of secondary Cu- and Fe-minerals, which are characterized by traces of native Au and Cu. The supergene enrichment zone hosts mainly chalcocite and covellite as well as minor cuprite and native copper (Figure 11).

Hematite and goethite are associated to pyrite and chalcopyrite oxidation (Figure 13a). Hematite is found only at the surface where it forms sheets and botryoidal to granular aggregates. In rock fractures or micro-cavities, hematite appears as radial and bushy aggregates of platy sheets, commonly with sericite and rutile. Goethite is the dominant mineral in the fault zones where it forms massive aggregates. In the oxidation zone, goethite replaces pyrite and chalcopyrite, forming pseudomorphs after pyrite and aggregates in micro-cavities, respectively.

Malachite and minor azurite are mostly present in the oxidation zone of the latite and in the phreatic breccia. Malachite appears as massive, botryoidal aggregates and acicular to tabular-prismatic crystals filling interstices and fractures in the rock, whereas azurite forms encrustations.

Cuprite increases with depth in the oxidation zone [46]. It is mainly found near the supergene enrichment zone at a depth of 90 to 92 m in veinlets with minor chalcocite and covellite. Native copper forms small disseminated grains (up to 50 μm in size) in cuprite. Chalcocite and covellite occur in the secondary enrichment zone where they are most abundant at depths between 90 and 100 m.

Although relatively rare in Greece, turquoise occurs on the eastern side of Ragian 1 Hill [57,58] (Figure 15a,b). It occurs in veinlets and encrustations exhibiting characteristic pale green-blue and forms hexagonal pseudomorphs after apatite [58]. In addition to turquoise, various minor occurrences of woodhouseite and phosphate carbonates, rich in large-ion lithophile elements (LILE) and HFSE (mainly Sr, Nb, Ce, Th, La, U), as well as senaite, are intergrown with sericite or they form in the rock interstices (Figure 15b).

The autunite group minerals, torbernite and meta-torbernite, occur as disseminations and encrustations in the oxidation zone of latite. On the eastern side of Ragian 1 Hill, pale green tabular torbernite and dark-green flat plates of meta-torbernite (crystals up to 3 mm in size) are locally present as disseminations in latite [44,59,60]. A significant concentration of torbernite occurs in drill hole D2 between 72 and 75 m [46] (Figure 3). Torbernite appears as disseminations, up to 3 mm in sizes, and as foliated to earthy aggregations of tabular crystals up to 3 cm in size [46].

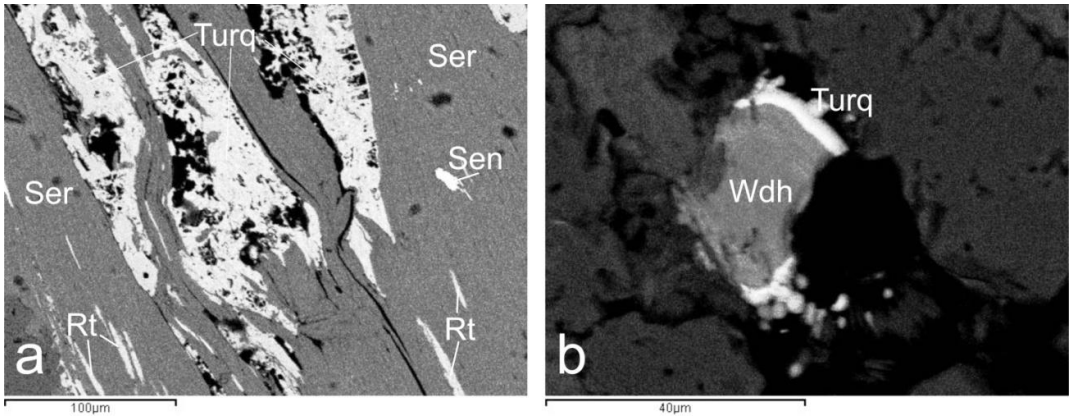

Figure 15. SEM back-scattered electron images of secondary minerals from the oxidation zone: (**a**) Turquoise (Turq), senaite (Sen), and rutile (Rt) along the cleavage of sericite (Ser); (**b**) Woodhouseite (Wdh) and turquoise (Turq) in a cavity in latite.

6.5. Geochemistry of Ore Mineralization

Based on the chemical analyses of 21 mineralized surface samples (Table 1), the Vathi porphyry system is locally enriched in Cu (avg: 2313 ppm), Mo (avg: 152 ppm), Au (avg: 0.46 ppm), U (avg: 31 ppm), Pb (avg: 120 ppm), Zn (avg: 55 ppm), and Ag (avg: 1 ppm). This enrichment in base and precious metals is spatially related to hydrothermal alteration and to the distribution of metallic minerals. On the surface, the highest grades of Au, Ag, Cu, Mo, Pb, Zn, and U are mainly associated with the intense sericitic alteration and oxidized D-type veins on the eastern side of the latite at Ragian 1 Hill (Figure 16). Weak anomalies of gold are present along and around stocks of quartz monzonite.

The propylitic alteration in latite generally contains a paucity of metal (only up to 116.8 ppm Cu, 5.16 ppm Mo, 36.3 ppb Au, 11.15 ppm U, 306.7 ppm Pb, 54.0 ppm Zn, and 0.7 ppm Ag; Table 1). Samples affected by sericitic alteration exhibit higher metal concentrations. The highest metal concentrations in samples VTH 6 and VTH 11 reach up to 9297 ppm Cu, 319.1 ppm Mo, 6996 ppb Au, 262.6 ppm U, 977.3 ppm Pb, 212 ppm Zn, and 4.2 ppm Ag (Table 1). This enrichment is associated with the sericitic alteration and secondary oxidation.

The phreatic breccia is also characterized by high U (40.5 ppm) and REE contents especially La (613.1 ppm), Ce (894.0 ppm), Pr (79.1 ppm), Nd (211.1 ppm), and Sm (23.4 ppm) (Tables 1 and 2). The highest concentrations of the REE are in samples from the sericitic alteration (97.7 ppm La, 160.02 ppm Ce, 20.26 ppm Pr, 93.1 ppm Nd, and 17.4 ppm Sm).

6.6. Fluid Inclusion Study

A fluid inclusion study was conducted on quartz from A- and E-type veins and on hydrothermal quartz grains related to sericitic alteration associated with the porphyry mineralization and the epithermal overprint, respectively. Samples of A-type veins cross-cutting quartz monzonite were obtained from the surface (Vath 31c) and from drill core H4 (Vath 40). Samples of E-type veins were collected from cataclasite at the surface (Vath 33) and from drill cores H4 (sample Vath 41) and H5 (sample Vath 42). Hydrothermal quartz in the sericitic alteration was derived from the surface (sample Vath 12a). D-type veins are devoid of fluid inclusions.

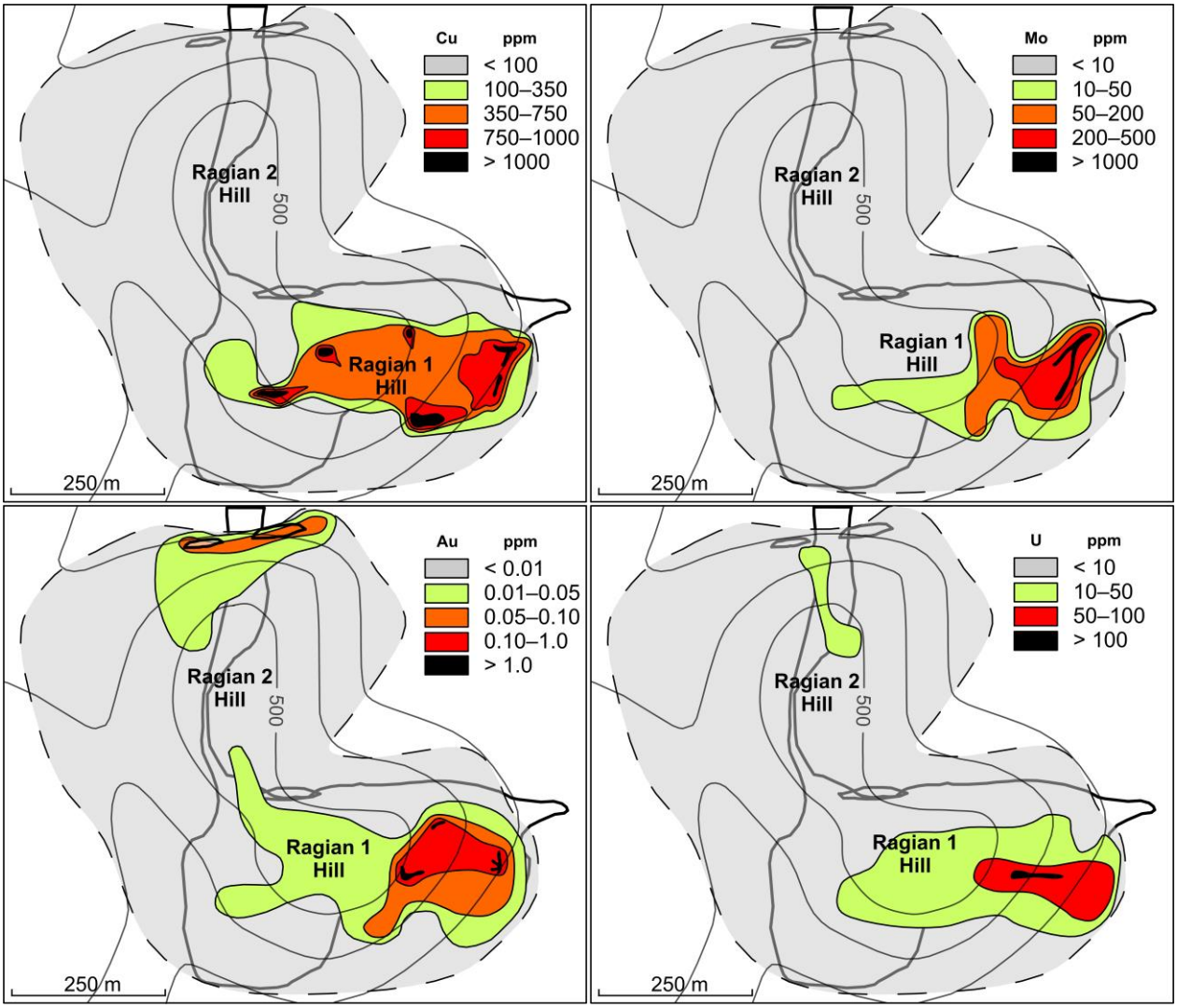

Figure 16. Distribution of copper, molybdenum, gold, and uranium in the Vathi porphyry-type deposit (see Figures 3 and 9).

Quartz in the veins and latite is mainly equigranular, anhedral, and it possesses a polygonal shape. The contacts among quartz grains form triple junctions with angles at ≈120° (Figure 17a). This implies that the quartz was extensively recrystallized so that the fluid inclusions largely migrated to grain boundaries [61]. As a result, fluid inclusions at Vathi are scarce, and only five of eight samples contained workable inclusions.

Where present, fluid inclusions are concentrated in clusters (Figure 17b) and are considered to be primary, on the basis of the criteria proposed by Roedder [62] and Goldstein and Reynolds [63]. These criteria include constant liquid to vapor ratios and similar shapes and sizes of the inclusions. Primary fluid inclusions found along growth zones of quartz crystals are rare, and their size is too small for microthermometry. Inclusions that occur in planes along healed fractures (Figure 17c) are considered to be secondary and possibly reflect fluid circulation associated with a late stage of fluid entrapment. The primary inclusions are elliptical to rounded and sometimes irregular in shape. Their maximum diameter is 35 μm, but the vast majority range in size from 5 to 15 μm.

On the basis of phase ratios observed at room temperature and phase transitions during homogenization, four types of fluid inclusions are present in the early-stage A-type veins and the hydrothermal quartz of the host rock: two-phase liquid-rich aqueous (Type 1), multiphase halite-bearing (Type 2), two-phase vapor-rich aqueous (Type 3), and one-phase vapor only (Type 4) inclusions.

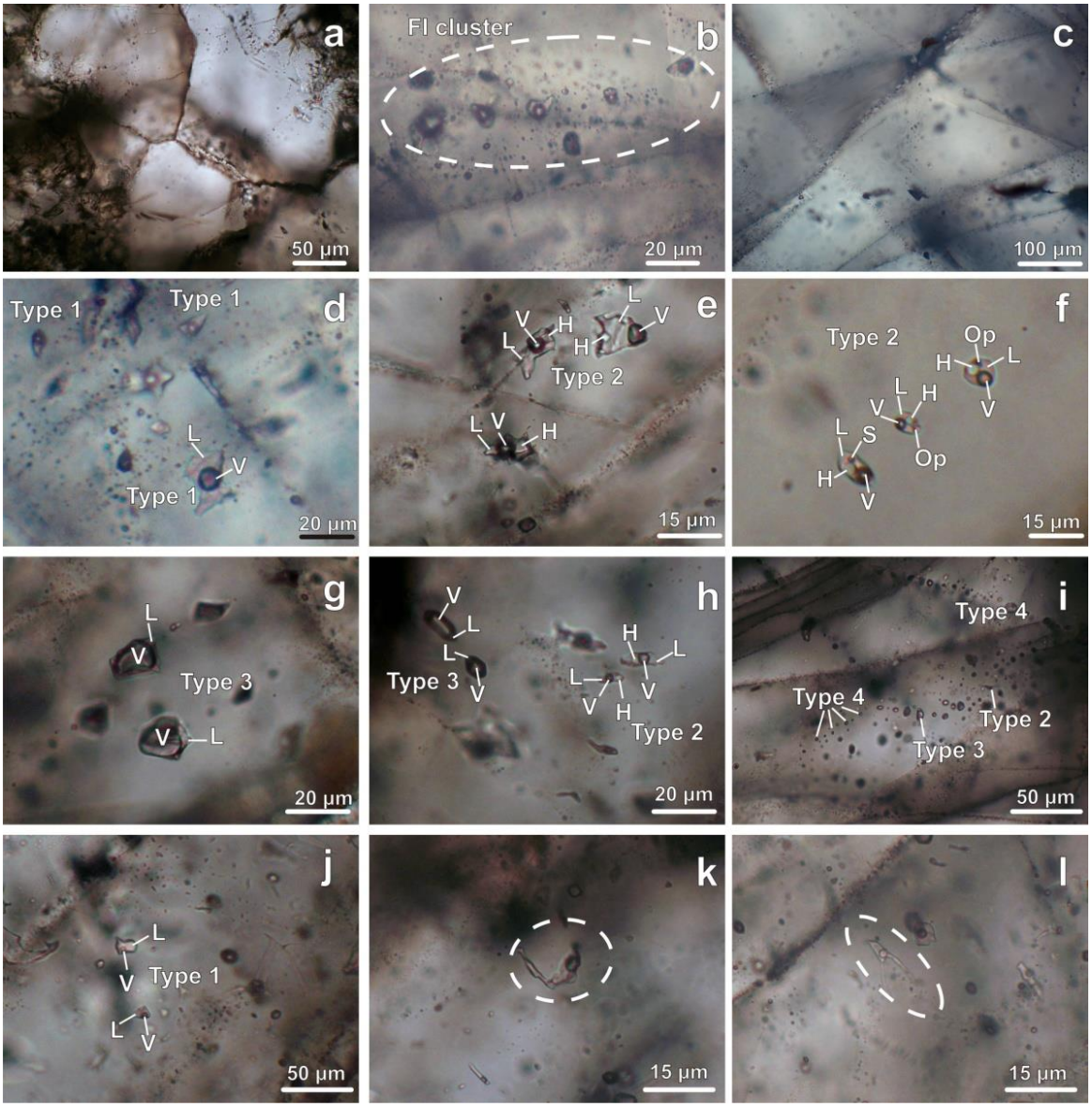

Figure 17. Photomicrographs of fluid inclusions in quartz from the Vathi deposit: (**a**) Equigranular quartz grains in association with the ore minerals, forming triple junctions with angles of ≈120°; (**b**) A cluster of primary two-phase liquid–vapor fluid inclusions; (**c**) Vapor-only secondary inclusions in planes along healed fractures; (**d**) Type 1 fluid inclusions from hydrothermal quartz grains in the sericitic alteration; (**e**) Type 2 three phase liquid–vapor–halite fluid inclusions; (**f**) Type 2 multiphase fluid inclusions containing halite, sylvite, and an opaque (possibly chalcopyrite or pyrite); (**g**) Type 3 vapor-rich inclusions; (**h**) Typical fluid inclusion assemblage in porphyry-style mineralization showing co-existing type 2 and 3 inclusions; (**i**) Type 2, 3, and 4 fluid inclusions; (**j**) A cluster of type 1 fluid inclusions in an epithermal vein; (**k**,**l**) Deformed and stretched fluid inclusions that leakage after trapping. FI = fluid inclusion; L = liquid; V = vapor; H = halite; S = sylvite; Op = opaque.

Type 1 two-phase aqueous inclusions contain a vapor bubble occupying 20–30 vol.% (Figure 17d), which homogenize into the liquid phase during heating. These inclusions occur in A-type veins and are rare and secondary in origin, although some primary inclusions occur in the hydrothermal quartz grains in latite.

Type 2 inclusions are multiphase and consist of liquid, vapor, and one or more daughter crystals consisting mostly of halite and rare sylvite, or other unidentified transparent daughter minerals or an opaque (Figure 17e–h). The vapor phase occupies 20–40 vol.% of the inclusions, which homogenize into the liquid phase. Halite and sylvite, where halite

is generally larger than sylvite, were identified by their colorless, isotropic cubic crystal morphology (Figure 17e,f). Halite dissolved at a higher temperature than sylvite during heating. The opaque phases (Figure 17f) are either cubic or triangular in shape and are possibly pyrite or chalcopyrite, respectively, but they do not dissolve during heating up to 600 °C.

Type 3 two-phase inclusions are dominated by a vapor bubble comprising 70–90 vol.% of the inclusions (Figure 17b,g,h) and homogenize into the vapor phase. They are the most common type of inclusion. Type 3 fluid inclusions commonly locally coexist with type 2 inclusions (Figure 17h). Type 4 inclusions are usually dark in color and consist mainly of vapor. They occur along healed fractures and are considered to be secondary in origin (Figure 17c,i).

None of the inclusions analyzed at the Vathi porphyry system contain visible liquid CO_2, and clathrate formation was not observed during freezing experiments. This excludes the presence of significant quantities of CO_2 (<2 mol.%).

Quartz in the epithermal veins contains few fluid inclusions, but where present, they are <20 μm in length. They are two-phase aqueous liquid–vapor inclusions (Type 1) containing a vapor bubble occupying 10–20 vol.% (Figure 17j). These inclusions homogenized into the liquid phase upon heating. Post-entrapment modifications, such as necking down or leakage, have affected this type of fluid inclusions (Figure 17k,l). They commonly occur along micro-cracks and demonstrate a variable liquid-to-vapor ratio. This is likely due to "stretching" processes during mechanical intracrystalline straining [64]. In order to eliminate the effects of the post-entrapment modifications, only inclusions with constant liquid-to-vapor ratios were selected for the microthermometric measurements.

Microthermometric data from 78 fluid inclusions in hydrothermal quartz and A-type veins from the Vathi porphyry system are summarized in Table 3. Eutectic ice-melting temperatures (Te) obtained from a few type 1 inclusions are concentrated around −22 °C, which suggests that NaCl is the dominant salt species in the inclusions [65]. Eutectic temperatures of type 3 inclusions were not possible to determine due to their small size.

Final ice melting temperatures of type 1 inclusions vary from −7.6 to −5.4 °C, indicating salinities of 8.4 to 11.2 wt % NaCl equiv [66]. Due to the small size (mainly 5–11 μm) of the meniscus liquid phase in type 3 inclusions, which made observation of the phase changes difficult, only a few freezing data could be obtained. On the basis of the freezing point depression (−14.1 to −6.4 °C), the salinities ranged from 9.7 to 18.5 wt % NaCl equiv.

Halite in type 2 fluid inclusions of A-type quartz veins dissolved at temperatures between 220 and 401 °C, corresponding to salinities of 32.7–47.2 wt % NaCl equiv. Salinity estimates based on the dissolution temperature of halite and sylvite in three type 2 inclusions yielded values between 28.4 and 36.7 wt % NaCl and 18.8 to 20.3 wt % KCl, which corresponds to a salinity of between 38.4 and 46.1 wt % NaCl equiv, respectively.

Homogenization temperatures (Th) for type 1 liquid-rich inclusions in quartz range from 311 to 392 °C (Figure 18). Type 2 liquid-rich halite-bearing fluid inclusions homogenized by disappearance of the vapor bubble after the halite crystal had disappeared at temperatures from 394 to >600 °C (the upper operating limit of the fluid inclusion stage). Homogenization temperatures of type 3 vapor-rich inclusions range from 335 to >600 °C. The majority of values of Th for type 2 and 3 fluid inclusions overlap between 390 and 540 °C and have a distinct maximum at ≈510 °C (Figure 18).

Microthermometric results for quartz in E-type epithermal veins were obtained from type 1 fluid inclusions in quartz (Table 3). Eutectic ice-melting temperatures range between −22 and −21 °C, suggesting that NaCl is the only dissolved salt in the fluid [65]. Final ice melting temperatures (−1.7 to −0.8 °C) correspond to salinities of 1.4 to 2.9 wt % NaCl equiv. Homogenization temperatures range from 205 to 259 °C, with a distinct maximum at ≈220 °C (Figure 18).

Table 3. Microthermometric data of the fluid inclusions in quartz of the A-type porphyry veins and the E-type epithermal veins from Vathi.

Sample	Vein Type	FI * Types	Th (°C)	Tm (ice) (°C)	Tm (NaCl) (°C)	Tm (KCl) (°C)	Salinity (wt % NaCl equiv *)
Vath 40	Porphyry A-type vein	2 (L+V+H→L)	320 to >600 (n = 11)	-	253–401 (n = 11)	105–125 (n = 2)	34.6–47.2
		3 (L+V→V)	335–515 (n = 23)	−13.4–−7.2 (n = 4)			10.7–17.4
Vath 31c	Porphyry A-type vein	2 (L+V+H→L)	324–>600 (n = 19)	-	220–374 (n = 19)	112 (n = 1)	32.7–44.3
		3 (L+V→V)	405 to >600 (n = 14)	−14.1–−6.4 (n = 2)	-	-	9.7–18.5
Vath 12a	Hydrothermal quartz in latite	1 (L+V→L)	311–392 (n = 7)	−7.6–−5.4 (n = 5)	-	-	8.4–11.2
Vath 41	Epithermal E-type vein	1 (L+V→L)	205–255 (n = 8)	−1.5–−0.9 (n = 3)	-	-	1.6–2.6
Vath 42	Epithermal E-type vein	1 (L+V→L)	212–259 (n = 5)	−1.7–−0.8 (n = 5)	-	-	1.4–2.9
Vath 33	Epithermal Catclasite	1 (L+V→L)	211–251 (n = 9)	−1.6–−0.9 (n = 9)	-	-	1.6–2.7

* FI = fluid inclusion, L = liquid phase, V = vapor phase, H = halite, equiv = equivalent, n = number of microthermometric analyses.

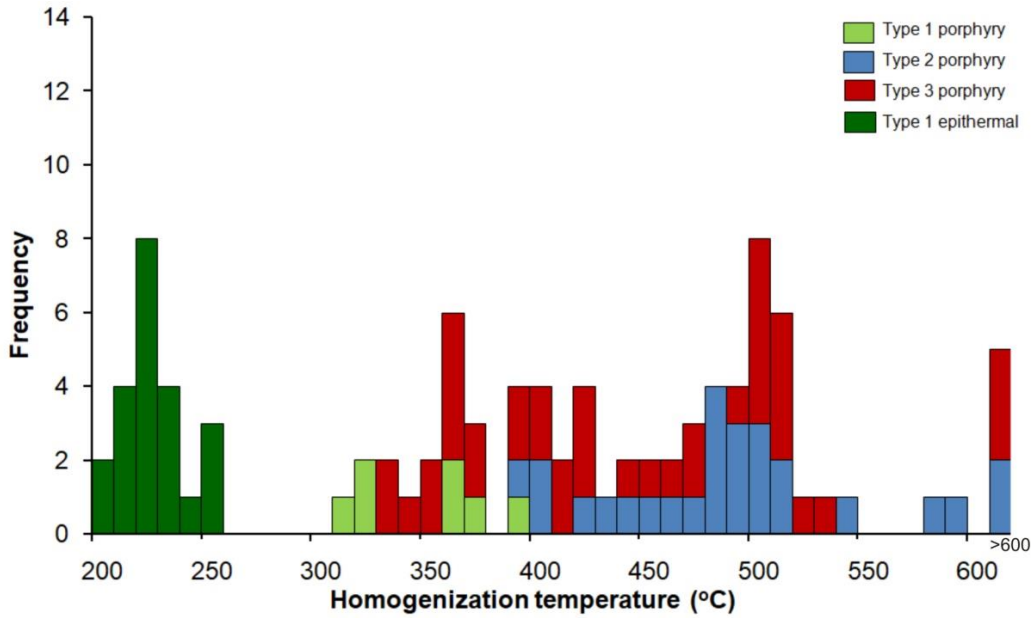

Figure 18. Homogenization temperatures of the fluid inclusions from the A- and E-type veins at Vathi.

7. Discussion

7.1. Geotectonic Setting, Structural Control, and Magma Emplacement

The magmatic complex at Vathi was emplaced during post-subduction tectonic extension. During the Miocene, several deep to shallow subvolcanic stocks, plugs, and dikes, which vary from intermediate to felsic compositions, intruded the metamorphic basement rocks in the Vathi area [16,45]. Their emplacement was controlled by regional structures

including E-W, NW-SE, and NE-SW trending faults, which also favored the formation of the porphyry-style mineralization by localizing the magmatic-hydrothermal fluid circulation (Figure 3; inset map).

The mineralization at Vathi is mainly hosted in latite, but it is genetically related to quartz monzonite, which intruded the older latite and the crystalline rocks of the Vertiskos Unit. The subvolcanic intrusion formed between 18 ± 0.5 and 17 ± 1 Ma, based on U-Pb zircon ages of Frei [16]. The microgranular and porphyritic texture and the elongate shape of the ore-related quartz monzonite are ascribed to fast ascending magma and subsequent crystallization at shallow depths set in an extensional regime. Melfos et al. [34] describe a similar mechanism for the origin of microgranite porphyry associated with the Maronia Cu-Mo deposit, NE Greece.

The presence of the phreatic breccia intruding the latite at Ragian 1 Hill, its ESE-WNW orientation, and the minor presence of quartz monzonite fragments suggest that quartz monzonite intruded the latite. This breccia was possibly formed when magmatic fluids were mixed with surface meteoric water during the late stages of the quartz monzonite intrusion, at the upper and marginal parts of the porphyry system [50,56].

7.2. Hydrothermal Alteration

Potassic and sericitic alteration is spatially related to the main stage of sulfide mineralization, whereas propylitic alteration hosts insignificant amounts of pyrite and chalcopyrite. The potassic alteration formed during the emplacement of the quartz monzonite and is characterized by the presence of quartz, hydrothermal biotite and K-feldspar, magnetite, chalcopyrite, bornite, molybdenite, and pyrite.

Propylitic alteration (epidote and chlorite) was likely coincident with the late stage of formation of the potassic alteration. Pyrite and chalcopyrite are found in trace amounts in the propylitic alteration, suggesting a slight increase in the sulfur fugacity of the hydrothermal fluids and/or a rise of the fluid temperature [67].

Sericitic alteration is expressed by the almost complete replacement of magmatic K-feldspar, clinopyroxene, hornblende, and biotite and by the extensive presence of sericite and quartz in the ground mass. Kaolinite, dolomite, and rutile constitute minor phases. Acicular to prismatic rutile crystals were formed as a result of Ti removal from precursor biotite during alteration [68]. The sericitic alteration overprints the potassic and propylitic alteration. The areas of sericitic alteration with the intense feldspar destructive textures possess relatively high sulfur content (S = ≈1.30 wt %). The magmatic fluid activity that resulted in the formation of this alteration zone during the late phases of the porphyry system was mainly controlled by the major E-W trending fault at the eastern part of Ragian 1 Hill. In this location, minor quartz veins and abundant mineralized D-type veins crosscut the host rocks.

7.3. Physicochemical Parameters of the Hydrothermal Fluids

Exsolution of hydrous fluids and silicate melts during the crystallization of the quartz monzonite at a shallow depth favored the hydraulic fracturing of the quartz monzonite and latite, which enhanced the permeability of the host rocks and the deposition of magnetite, chalcopyrite, bornite, molybdenite, and pyrite in A-type veins, fractures, and as disseminations in the host rock. This stage of mineralization is associated with the potassic alteration.

Fluid inclusions in A-type quartz veins at Vathi show that quartz and related metallic mineralization formed as a result of phase separation from an initial high temperature (at least >600 °C), featuring moderate-salinity supercritical magmatic fluid (Figures 19 and 20) under boiling conditions during the ascent and cooling of the fluids. The rapid drop in temperature and pressure favored fluid immiscibility in these veins, resulting in a saline brine (33–47 wt % NaCl equiv; type 2) and a co-existing lower salinity (10–19 wt % NaCl equiv; type 3) low-density vapor-rich fluid at lithostatic pressures that homogenize over the same temperature range, mainly between 390 and 540 °C. This association, plus the

presence of type 4 vapor-rich inclusions, suggests that the potassic alteration was associated with fluid boiling (Figure 19) as has been described elsewhere [62,66,69,70].

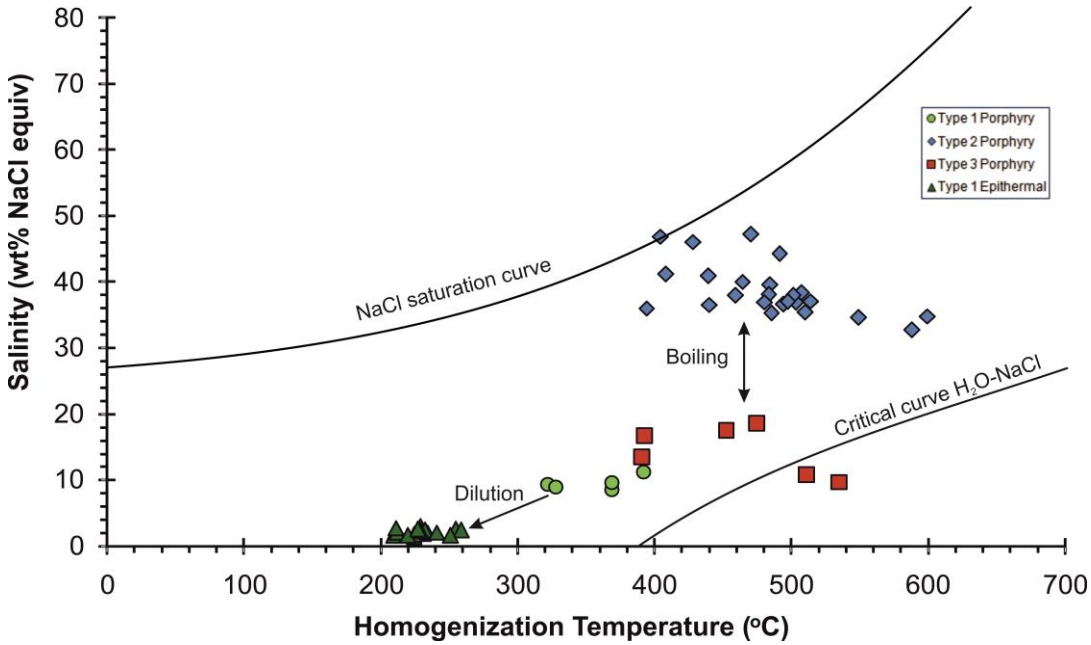

Figure 19. Salinity versus homogenization temperature plot of the fluid inclusions at Vathi.

The presence of halite and sylvite in fluid inclusions indicates that the ore-bearing fluid in A-type veins was saturated in NaCl and KCl, as well as the likely presence of chalcopyrite and pyrite in type 2 inclusions, shows that the fluids were hypersaline and that Cu at Vathi was likely precipitated by the condensation of metal-rich brines.

Fluid inclusions trapped from boiling fluids do not require pressure corrections, and the measured homogenization temperatures represent trapping temperatures [62,70]. Trapping pressures of co-existing type 2 and 3 fluid inclusions in A-type veins at Vathi range from 248 to 646 bars, which were estimated using the equation of state of Zhang and Frantz [71] and homogenization temperatures. This corresponds to a depth of ore formation between 1.0 and 2.6 km assuming lithostatic conditions (Figure 20). The estimated densities of the hydrothermal fluids are >0.77 g cm^{-3} for the highly saline liquid-rich (type 2) fluids, and <0.78 g cm^{-3} for the moderate-salinity vapor-rich (type 3) fluids.

Fluid boiling can cause extensive hydraulic fracturing of the wall rocks and result in mixing of ascending boiling magmatic fluid with meteoric water at the ductile to brittle transition under hydrostatic pressures [72]. The lower temperature (310–390 °C) and less saline (8–11 wt % NaCl equiv) type 1 liquid-rich fluid inclusions in the hydrothermal quartz of latite at Vathi (Figure 19) likely represents a late fluid that was associated with decompression under hydrostatic pressures (Figure 20). This decompression was caused by extensive hydrofracturing and generated the fractures associated with the metallic mineralization at Vathi [69], which is associated with the sericitic alteration.

Fluid inclusions from the E-type epithermal veins are characterized by low salinity (1.4–2.9 wt % NaCl equiv) and relatively low Th ranging between 205 and 259 °C, with a maximum at ≈220 °C (Figures 19 and 20). These fluid inclusions formed during the final stage of the magmatic–hydrothermal evolution of the system and represent a dilute fluid resulting from the mixing of a moderate saline fluid with circulating meteoric water in the epithermal stage. These non-boiling fluids are associated with the assemblage sphalerite + galena + arsenopyrite ± stibnite ± tennantite ore. Therefore, pressures obtained for non-boiling fluid inclusion assemblages represent minimum trapping values, and the pressure correction is estimated to be <10 °C, since these veins probably formed at shallow

depths (e.g., [73]). The estimated minimum trapping pressures of the Vathi epithermal veins range from 100 to 244 bars, indicating a depth between 110 and 250 m under hydrostatic conditions. The estimated densities of the hydrothermal fluids in these veins are >0.79 g cm^{-3}.

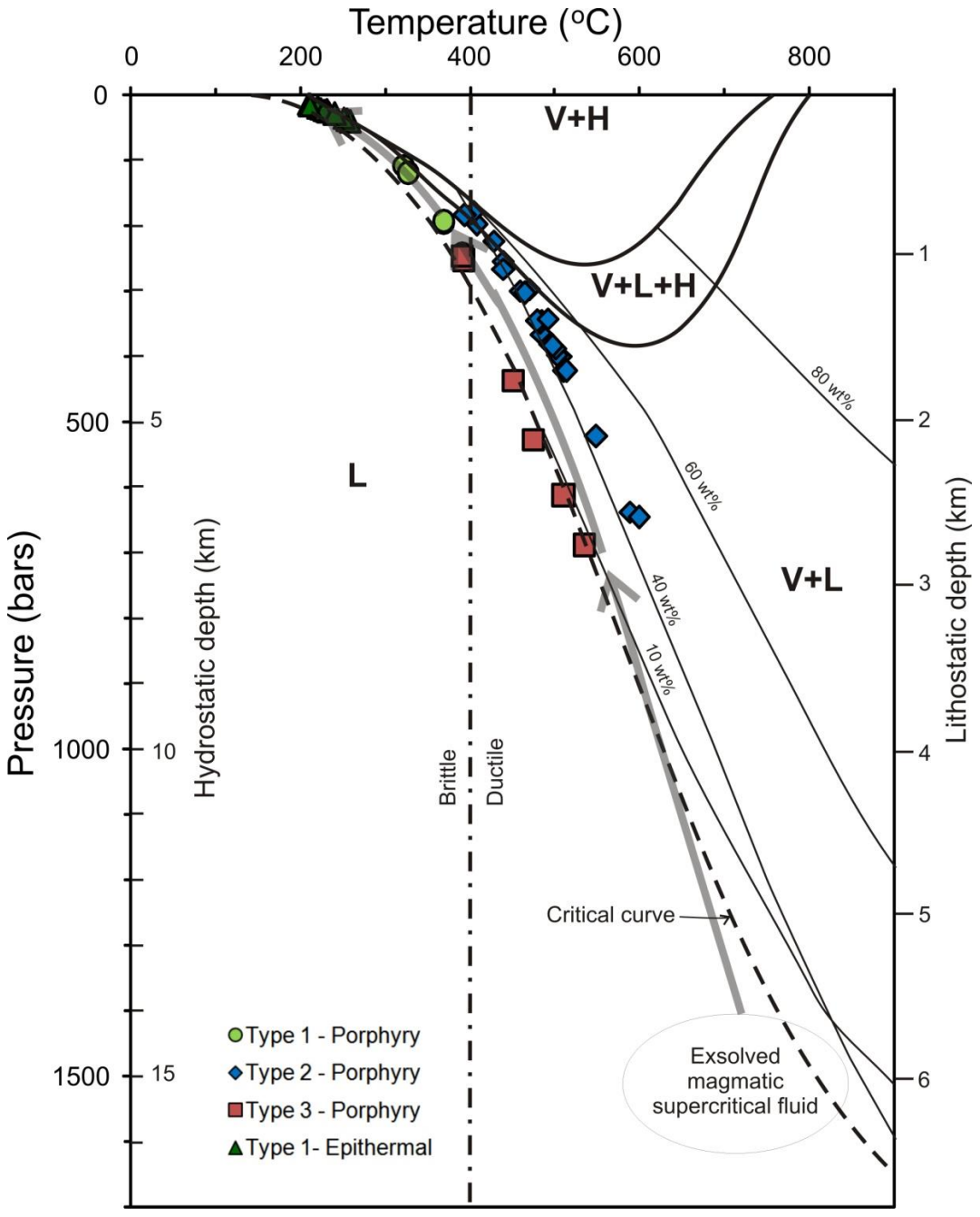

Figure 20. Pressure–temperature diagram and phase relations in the H_2O–NaCl system at lithostatic and hydrostatic conditions (adapted from [74]) showing the distribution of the Type 1, 2, and 3 fluid inclusions at Vathi. Depths assuming a 2.5 g/cm^{-3} lithostatic load and a 1 g/cm^{-3} hydrostatic load are also shown. Isopleths of NaCl in liquid in the two-phase vapor + liquid field are shown by the light weighted lines. The plastic–brittle transition lies at about 400 °C [75]. The gray heavy arrows show the proposed fluid path based on the fluid inclusion data. V = vapor, L = liquid, H = halite.

7.4. Source of Metals

Phase separation promotes Au deposition in porphyry systems, which follows the deposition of Cu at high temperatures [76,77]. In addition, Au precipitation in phreatic breccias is favored by the permeable textures created by the periodic catastrophic release of the build-up of volatiles [56]. This could also be the case for the Au enrichment during the formation of the Vathi breccia (724 ppb Au). At Vathi, gold is also related to the oxidized D-type veins, which occur in the sericitic alteration (6996 ppb Au). A similar relationship between high Au contents and D-type mineralized veins was reported by Voudouris et al. [78], where gold is found as inclusions in pyrite in the Pagoni Rachi Cu-Mo-Re-Au deposit in northern Greece.

Molybdenum at Vathi was precipitated near and below a depth of 166 m after Cu was precipitated, while Fe, Pb, Zn, and As are enriched in the upper, outer, and adjacent areas of the quartz monzonite and was related to the epithermal stage. Frei [16], based on Pb isotope compositions, has shown that the enrichment of Cu, Pb, and Zn at Vathi is associated with crustal rocks assimilation from magma.

The quartz-monzonite and latite at Vathi are enriched in Sr (Vath 41: 1269.1 ppm, Vath 42: 1173.2 ppm), Rb (Vath 41: 165.3 ppm, Vath 42: 120.1 ppm), and Ba (Vath 41: 1513.8 ppm, Vath 42: 867.8 ppm) (Table 2). These elements are lithophile and incompatible in the mantle, and the enrichment of these elements could be related to differentiation of the parental magma and the subsequent interaction with crustal rocks, as well as to the onset of significant plagioclase fractionation [79,80]. In this regard, Sr values are considered more enriched, with respect to reported values from intermediate to evolved magmas (<100 ppm) [80]. Moreover, the enrichment in high field strength elements (HFSE; Zr, Hf, Nb, and Ta) is likely the result of limited assimilation of crustal rocks as the magma differentiated [79].

A significant enrichment is also observed in the REE: La (up to 613.1 ppm), Ce (up to 894 ppm), Pr (up to 79.1 ppm), Nd (up to 211.1 ppm), and Gd (up to 12.7 ppm), as well as in Ti (up to 7040 ppm) and P (up to 1340 ppm) (Table 2). These geochemical anomalies could suggest that the Vathi deposit shares several characteristics in common with alkaline igneous rock-related porphyry deposits [81].

Uranium exhibits moderately to highly enriched concentrations in the magmatic rocks in the Vathi area (14 to 106 ppm). In the phreatic breccia and along the mineralized tectonic structures, the high U content (up to 328 ppm) is manifested by the presence of autunite-group minerals, torbernite and meta-torbernite. Uranium enrichment is rather an uncommon characteristic of porphyry systems associated with calc-alkaline igneous rocks [82]. On the contrary, U tends to be enriched in porphyry deposits related to alkaline intrusions [82,83].

At the Vathi area, the enrichment in U was likely associated with the final stages of crystallization of the mildly alkaline magma combined with movement along deep-seated faults. Rupturing of the intrusive cupola was likely associated with fluid exsolution and the accumulation of a magmatic fluid enriched in U. Fluid exsolution was favored by deep-seated faults, while a network of fractures enhanced rock permeability resulting in the formation of secondary torbernite. Rice et al. [83] described a similar mechanism that resulted in the enrichment of U in the alkaline igneous rock-related porphyry molybdenum system at Central City, Colorado.

7.5. Origin of the Vathi Deposit

In the early Cenozoic, melts enriched in volatiles, Cu, and other chalcophile metals were extracted from the subducted oceanic crust in northern Greece [84]. These melts ascended into the overlying delaminated crust, inducing partial melting. This melting resulted in significant crustal rock assimilation and produced magmas of calc-alkaline to high K-calc-alkaline and of shoshonitic affinities, which then intruded the upper crust, resulting in post-collisional back-arc magmatism [26]. An extensional tectonic regime, characterized by detachment and strike–slip faults in transpressional and transtensional

tectonic settings, characterizes the Oligocene–Miocene deformation of the upper crust [19]. This deformation structurally controlled the formation of the I-type plutonic rocks and the related intrusive and extrusive magmatic rocks [84].

The oxidizing character of the magma that formed the ore deposit and the quartz monzonite association with porphyry copper-style mineralization have been previously mentioned for Vathi [16]. The Al_2O_3/TiO_2 and V/Sc ratios for unaltered and altered samples, respectively, can be applied to assess the magmatic fertility and prospectivity of Cu and Au [85]. Using the criteria of Loucks [85], samples of quartz monzonite and latite at Vathi were plotted as functions of Al2O3/TiO2 versus SiO2 and V/Sc versus SiO_2 (Figure 21a,b). The V/Sc ratio of samples from Vathi ranges from 10 to 50.91 and 11.84 to 17.08 for quartz monzonite and latite, respectively (Table 2), and they fall in the category of prospective Cu-Au deposits worldwide as characterized by V/Sc >10 [85]. In both Figure 21a,b, the Vathi samples plot in the fields of more productive Cu and Cu + Au intrusive rocks.

At the Vathi area, the ore-forming magma was focused at the intersection of major regional structures in the upper crust at a depth of >3 km where it crystallized to form stocks, plugs, and dikes of intermediate to felsic composition (Figure 3; inset map). The major and minor structural features provided a vertically extensive dilatant network, which favored the evolution of the magmatic–hydrothermal porphyry system at Vathi (Figure 22a).

Disseminations, veins, veinlets, and small aggregates of magnetite + chalcopyrite + pyrite + bornite + molybdenite formed in the potassic alteration at Vathi. Volatile fluids migrated upward from the monzonitic magma through fractures. The initial high-temperature parental magmatic fluid cooled from 540 to 390 °C and decompressed at approximately 646 to 248 bars, which resulted in phase separation at a depth of 1 to 2.6 km (assuming lithostatic conditions). The resulting moderate-density vapor and saline brine fluids interacted with the surrounding host rocks to form potassic alteration, A-type veins, and associated Cu-Mo-Au mineralization (Figure 22a). In addition, the mixing of magmatic fluids and meteoric water during this stage resulted in boiling and phreatic brecciation. During the late stages of potassic alteration, propylitic alteration was developed, overprinting both the latite and the quartz monzonite (Figure 22b).

Later, the vapor phase formed synchronously with the potassic alteration stage and continued to move upwards, cooling and mingling with meteoric water to form an acidic moderate-salinity (8–11 wt % NaCl equiv) aqueous fluid at lower temperatures (310–390 °C). Sericitic alteration developed from these fluids along brittle fault zones (Figure 22c). The secondary porosity of the latite was further enhanced by extended hydraulic fracturing favoring the formation of a network of cracks in the latite and the quartz monzonite. Within this network, the pyritic mineralization and D-veins associated with gold were developed.

During the late epithermal stage, a low-salinity fluid (1.4–2.9 wt % NaCl equiv) was generated at relatively low Th (205 and 259 °C). This fluid represents a mixture of a moderately saline fluid with circulating meteoric waters at a depth of 110 to 250 m under hydrostatic conditions, which formed the E-type veins and the attendant sphalerite + galena + arsenopyrite ± stibnite ± tennantite mineralization (Figure 22d). These minerals are common in the late stages of many porphyry systems and are the result of Zn, Pb, As, and Sb accumulation in the residual ore-forming solution, commonly as late-stage epithermal E-type veins [55,56].

The assemblage pyrite + pyrrhotite + chalcopyrite at Vathi is a rather uncommon paragenesis in porphyry systems. In reduced porphyry systems, the low solubility of S and Cu, the predominance of S^{2-}, and the depletion in Cl^- favor the formation of massive pyrrhotite in temperatures between 350 and 600 °C [86–88]. However, pyrrhotite related to oxidized Cu-Au-porphyry systems has been reported from the biotite-actinolite alteration zones of alkaline igneous rock-related porphyry systems, peripheral to porphyry-Au deposit quartz stockwork veins, and they are caused by the interaction between late

chlorite-illite-quartz alteration and carbonaceous wall rocks [56,88]. At Vathi, it is likely that the formation of pyrrhotite is due to a lower sulfur fugacity of the ore fluid.

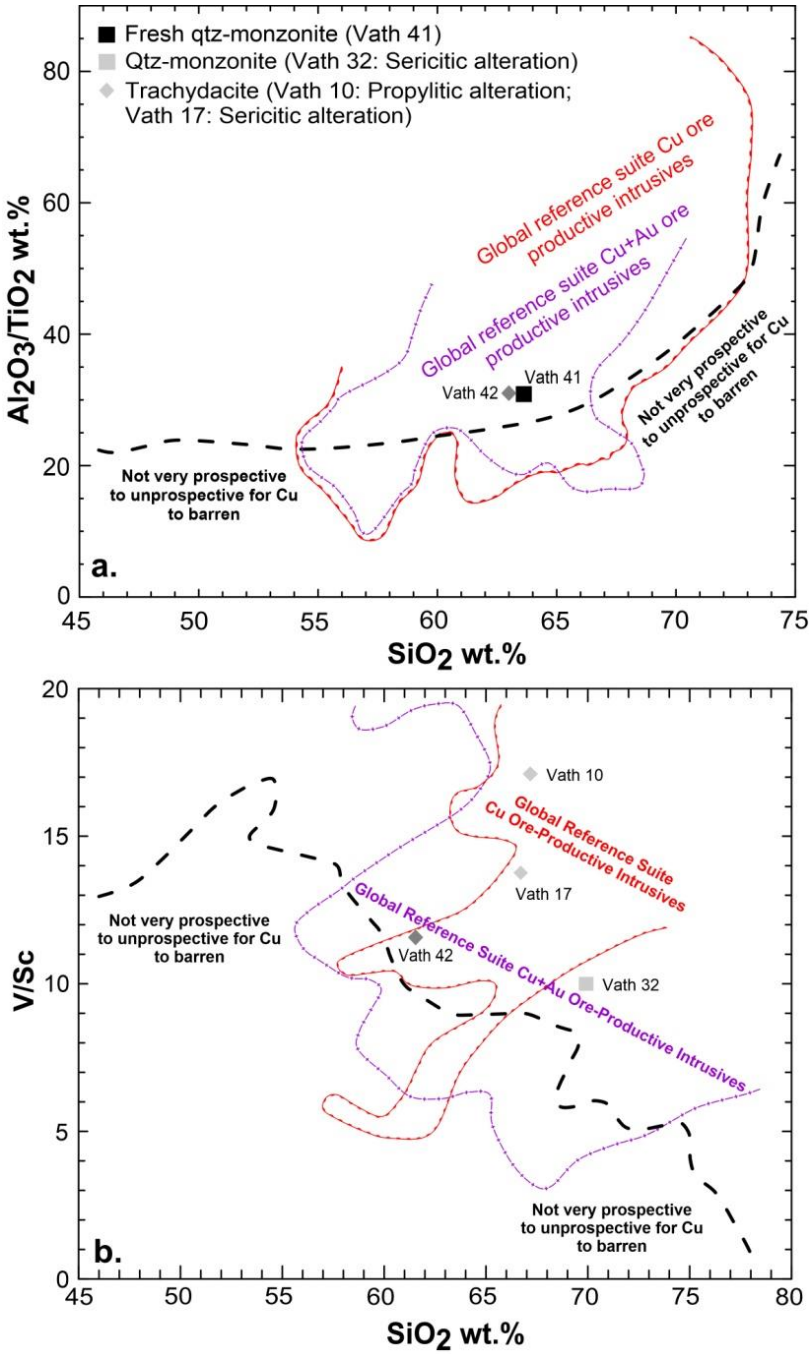

Figure 21. Whole-rock Al_2O_3/TiO_2 versus SiO_2 wt % and V/Sc ratios versus SiO_2 wt % of the Cu and Cu + Au ore for productive versus not very productive to unproductive barren intrusive rocks (modified after [85]): (**a**) A fresh quartz monzonite sample (Vath41: Al_2O_3/TiO_2 = 32.35) and a latite sample (Vath 42: Al_2O_3/TiO_2 = 31.63) affected by propylitic alteration plot occurs in the area of fertile and prospective Cu-Au ore deposits; (**b**) Prospective Cu-Au deposits are characterized by V/Sc > 10 ratios. Samples of quartz monzonite (Vath 32: V/Sc = 10.0) and latite (Vath 10: V/Sc = 17.08, Vath 42: V/Sc = 11.84) plot among the scatter range of the magmatically fertile and prospective Cu-Au ore deposits. Sample Vath 41 has a V/Sc ratio of 50.91 and plots outside the range shown in the diagram.

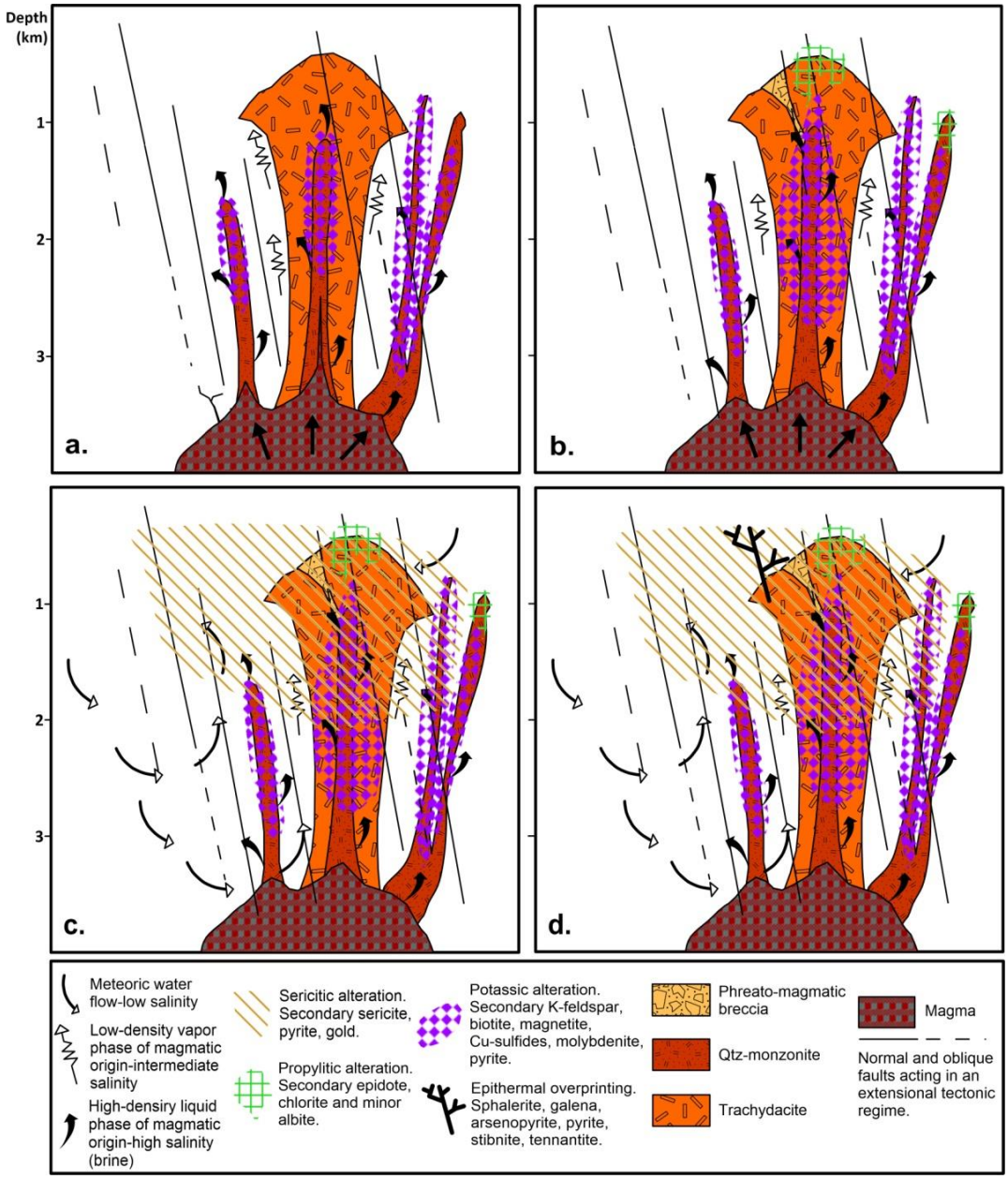

Figure 22. Schematic model of the formation of magmatic rocks, hydrothermal alteration, and ore mineralization at Vathi along an N-S cross-section: (**a**) Regional structural settings promote the fast ascent of the magmas (the position of faults is indicative) to form the quartz monzonite intrusions. Magmatic fluid exsolves from magma and flows upwards undergoing phase separation to form co-existing vapor and brine. As these fluids cool, they result in the potassic alteration and the related ore mineralization; (**b**) At the late stage of formation of the potassic alteration, magmatic fluids propylitize the latite and the quartz monzonite; (**c**) As the system cools, the vapor phase condenses and mixes with meteoric water, resulting in a late sericitic alteration that overprints potassic and propylitic alteration; (**d**) A new pulse of a low-salinity fluid of meteoric origin flows along the brittle fault zone to form the epithermal alteration and the late-stage metallic mineralization.

8. Summary and Conclusions

The Vathi porphyry Cu-Au ± Mo mineralization occurs in the northern part of the Oligocene-Miocene Serbo-Macedonian metallogenic province. The mineralization is mainly hosted in latite and is genetically associated with the intrusion of quartz monzonite (18 to 17 Ma). The quartz monzonite appears as fault-controlled, narrow, elongated stocks, while latite forms a plug-shaped body. These two rocks are silica-saturated and exhibit alkali-

calcic to slightly alkaline chemical affinities. A phreatic breccia crosscuts the latite and was likely formed during the intrusion of the quartz monzonite. Three major fault groups trending E-W, NW-SE, and NE-SW characterize the regional structures, which controlled the emplacement of the intrusions in the crystalline basement of the Vertiskos Unit. The quartz monzonite and latite were affected by potassic and propylitic alteration that were subsequently overprinted by sericitic alteration. The potassic alteration is associated with the ore assemblage pyrite + chalcopyrite + bornite + molybdenite + magnetite in M- and A-type veins, and the propylitic alteration is related to pyrite + chalcopyrite, while the later sericitic alteration is associated with the assemblage pyrite + chalcopyrite + native gold ± tetradymite in D-type veins. The assemblage sphalerite + galena + arsenopyrite + pyrrhotite + pyrite ± stibnite ± tennantite is related to a subsequent epithermal overprinting event. The metallic mineralization is enriched in Cu (average 2313 ppm), Mo (average 152 ppm), Au (average 0.46 ppm), and U (average 31 ppm). A local enrichment in some REEs (up to 613 ppm La, 894 ppm Ce, 79 ppm Pr, 211 ppm Nd and 23 ppm Sm) is attributed to the phreatic breccia and to secondary supergene mineralization. Fluid inclusion data indicate that A-type porphyry style veins were deposited at 390–>600 °C and at pressures up to 646 bars (<2.6 km depth) from boiling hydrothermal fluids. This process resulted in the generation of coexisting moderately saline (9.7–18.5 wt % NaCl equiv.) and highly saline (32.7–47.2 wt % NaCl equiv.) fluids. Sericitic alteration, D-type veins, and related pyrite + pyrrhotite + chalcopyrite mineralization are associated with a moderately saline fluid (8.4–11.2 wt % NaCl equiv) that formed as a result of condensation of vapor-rich fluids between 311 and 392 °C. At lower temperatures (205–259 °C), a less saline (1.4–2.9 wt % NaCl equiv.) fluid formed, which deposited late epithermal E-type veins and attendant mineralization. The anomalous enrichments in U and REE and the alkaline character of magmatism are possible indicators that Vathi shares several characteristics in common with alkaline igneous rock-related porphyry deposits.

Author Contributions: Conceptualization, C.L.S. and V.M.; data curation, C.L.S. and V.M.; investigation, C.L.S. and V.M.; methodology, C.L.S. and V.M.; software, V.M.; visualization, C.L.S. and V.M.; validation, P.V., P.G.S., L.P., A.C., and A.F.; writing—original draft preparation, C.L.S.; writing—review and editing, V.M., P.V., P.G.S., L.P., A.C., C.M., K.G., and A.F.; funding acquisition, C.L.S. All authors have read and agreed to the published version of the manuscript.

Funding: This research was funded by the Society of Economic Geologists Foundation (SEGF) Student Research Grants Program via the Hugh E. McKinstry Fund.

Institutional Review Board Statement: Not applicable.

Informed Consent Statement: Not applicable.

Data Availability Statement: Data is contained within the article.

Acknowledgments: José Perelló is sincerely thanked for his reviews and constructive comments on an earlier version of this manuscript. The associate editor and two anonymous reviewers are kindly thanked for editorial handling and for providing comments that significantly improved the manuscript.

Conflicts of Interest: The authors declare no conflict of interest.

References

1. Arvanitidis, N.D. New metallogenetic concepts and sustainability perspectives for non-energy metallic minerals in Central Macedonia, Greece. *Bull. Geol. Soc. Greece* **2010**, *43*, 2437–2445. [CrossRef]
2. Tsirambides, A.; Filippidis, A. Metallic mineral resources of Greece. *Cent. Eur. J. Geosci.* **2012**, *4*, 641–650. [CrossRef]
3. Tsirambides, A.; Filippidis, A. Gold metallogeny of the Serbomacedonian-Rhodope metallogenic belt (SRMB). *Bull. Geol. Soc. Greece* **2016**, *50*, 2037–2046. [CrossRef]
4. Goodenough, K.M.; Schilling, J.; Jonsson, E.; Kalvig, P.; Charles, N.; Tuduri, J.; Deady, E.A.; Sadeghi, M.; Schiellerup, H.; Müller, A.; et al. Europe's rare earth element resource potential: An overview of REE metallogenetic provinces and their geodynamic setting. *Ore Geol. Rev.* **2016**, *72*, 838–856. [CrossRef]

5. Melfos, V.; Voudouris, P.C. Geological, mineralogical and geochemical aspects for critical and rare metals in Greece. *Minerals* **2012**, *2*, 300–317. [CrossRef]
6. Melfos, V.; Voudouris, P. Cenozoic metallogeny of Greece and potential for precious, critical and rare metals exploration. *Ore Geol. Rev.* **2017**, *89*, 1030–1057. [CrossRef]
7. Baker, T. Gold±copper endowment and deposit diversity in the Western Tethyan magmatic belt, southeast Europe: Implications for exploration. *Econ. Geol.* **2019**, *114*, 1237–1250. [CrossRef]
8. Voudouris, P.; Mavrogonatos, C.; Spry, P.G.; Baker, T.; Melfos, V.; Klemd, R.; Haase, K.; Repstock, A.; Djiba, A.; Bismayer, U.; et al. Porphyry and epithermal deposits in Greece: An overview, new discoveries, and mineralogical constraints on their genesis. *Ore Geol. Rev.* **2019**, *107*, 654–691. [CrossRef]
9. Mavrogonatos, C.; Voudouris, P.; Berndt, J.; Klemme, S.; Zaccarini, F.; Spry, P.G.; Melfos, V.; Tarantola, A.; Keith, M.; Klemd, R.; et al. Trace elements in magnetite from the Pagoni Rachi porphyry prospect, NE Greece: Implications for ore genesis and exploration. *Minerals* **2019**, *9*, 725. [CrossRef]
10. Voudouris, P. Comparative mineralogical study of Tertiary Te-rich epithermal and porphyry systems in northeastern Greece. *Miner. Petrol.* **2006**, *87*, 24–275. [CrossRef]
11. Voudouris, P.; Spry, P.G.; Melfos, V.; Alfieris, D. Tellurides and bismuth sulfosalts in gold occurrences of Greece: Mineralogy and genetic considerations. In *Au-Ag Telluride-Selenide Deposits Field Workshop of IGCP-486, Proceedings Volume*; Kari, K., Kojonen, K.K., Cook, N.J., Juhani Ojala, V., Eds.; Geological Survey of Finland: Espoo, Finland, 2007; pp. 85–94.
12. Voudouris, P.C.; Spry, P.G.; Mavrogonatos, C.; Sakellaris, G.A.; Bristol, S.K.; Melfos, V.; Fornadel, A.P. Bismuthinite derivatives, lillianite homologues and bismuth sulfotellurides as indicators of gold mineralization in the Stanos shear-zone related deposit, Chalkidiki, Northern Greece. *Can. Mineral.* **2013**, *51*, 119–142. [CrossRef]
13. Bristol, S.K.; Spry, P.G.; Voudouris, P.C.; Melfos, V.; Mathur, R.D.; Fornadel, A.P.; Sakellaris, G.A. Geochemical and geochronological constraints on the formation of shear-zone hosted Cu-Au-Bi-Te mineralization in the Stanos area, Chalkidiki, northern Greece. *Ore Geol. Rev.* **2015**, *66*, 266–282. [CrossRef]
14. Stergiou, C.; Melfos, V.; Voudouris, P.; Michailidis, K.; Spry, P.; Chatzipetros, A. Hydrothermal alteration and structural control of the Vathi porphyry Cu-Au- Mo-U ore system, Kilkis district, N. Greece. In *Scientific Annals of the School of Geology*; Kantiranis, N., Ed.; Aristotle University of Thessaloniki: Thessaloniki, Greece, 2016; Volume 105, pp. 69–74.
15. Stergiou, C.L.; Melfos, V.; Voudouris, P. *A Review on the Critical and Rare Metals Distribution throughout the Vertiskos Unit, N. Greece*; MDPI: Basel, Switzerland, 2018. [CrossRef]
16. Frei, R. Isotope (Pb, Rb-Sr, S, O, C, U-Pb) Geochemical Investigations on Tertiary Intrusives and Related Mineralizations in the Serbomacedonian Pb-Zn, Sb+Cu-Mo Metallogenic Province in Northern Greece. Ph.D. Thesis, Swiss Federal Institute of Technology (ETH) Zurich, Zurich, Switzerland, 1992.
17. Kydonakis, K.; Brun, J.P.; Sokoutis, D.; Gueydan, F. Kinematics of Cretaceous subduction and exhumation in the western Rhodope (Chalkidiki block). *Tectonophysics* **2015**, *665*, 218–235. [CrossRef]
18. Ross, J.; Voudouris, P.; Melfos, V.; Vaxevanopoulos, M. Mines, Metals and Money: Ancient World Studies in Science, Archaeology and History. In *Metallurgy in Numismatics*; Sheedy, K.A., Davis, G., Eds.; Royal Numismatic Society Special Publication: London, UK, 2018; Volume 6, pp. 9–21.
19. Kilias, A.; Falalakis, G.; Mountrakis, D. Cretaceous-Tertiary structures and kinematics of the Serbomacedonian metamorphic rocks and their relation to the exhumation of the Hellenic hinterland (Macedonia, Greece). *Int. J. Earth Sci.* **1999**, *88*, 513–531. [CrossRef]
20. Himmerkus, F.; Reischmann, T.; Kostopoulos, D. Serbo-Macedonian revisited: A Silurian basement terrane from northern Gondwana in the Internal Hellenides, Greece. *Tectonophysics* **2009**, *473*, 20–35. [CrossRef]
21. Kilias, A.D.; Vamvaka, A.; Falalakis, G.; Sfeikos, A.; Papadimitriou, E.; Gkarlaouni, C.H.; Karakostas, B. The Mesohellenic Trough and the Paleogene Thrace Basin on the Rhodope Massif, their Structural Evolution and Geotectonic Significance in the Hellenides. *J. Geol. Geosci.* **2015**, *4*, 198. [CrossRef]
22. Schmid, S.M.; Fügenschuh, B.; Kounov, A.; Matenco, L.; Nievergelt, P.; Oberhänsli, R.; Pleuger, J.; Schefer, S.; Schuster, R.; Tomljenović, B.; et al. Tectonic units of the Alpine collision zone between Eastern Alps and western Turkey. *Gondwana Res.* **2020**, *78*, 308–374. [CrossRef]
23. Bonev, N.; Dilek, Y.; Hanchar, J.M.; Bogdanov, K.; Klain, L. Nd-Sr-Pb isotopic composition and mantle sources of Triassic rift Units in the Serbo-Macedonian and the western Rhodope Massifs (Bulgaria-Greece). *Geol. Mag.* **2012**, *149*, 146–152. [CrossRef]
24. Abbo, A.; Avigad, D.; Gerdes, A. Crustal evolution of peri-Gondwana crust into present day Europe: The Serbo-Macedonian and Rhodope massifs as a case study. *Lithos* **2019**, *356*, 105295. [CrossRef]
25. Perugini, D.; Poli, G.; Christofides, G.; Eleftheriadis, G.; Koroneos, A.; Soldatos, T. Mantle-derived and crustal melts dichotomy in northern Greece: Spatiotemporal and geodynamic implications. *Geol. J.* **2004**, *39*, 63–80. [CrossRef]
26. Pe-Piper, G.; Piper, D.J. Unique features of the Cenozoic igneous rocks of Greece. In *Postcollisional Tectonics and Magmatism in the Mediterranean Region and Asia*; Dilek, Y., Pavlides, S., Eds.; Special Papers; Geological Society of America: Boulder, CO, USA, 2006; Volume 409, pp. 259–282.
27. Kockel, F.; Mollat, H.; Gundlach, H. Hydrothermally altered and (copper) mineralized porphyritic intrusions in the Serbo-Macedonian Massif (Greece). *Miner. Depos.* **1975**, *10*, 195–204. [CrossRef]

28. Pe-Piper, G.; Piper, D.J. *The Igneous Rocks of Greece: Anatomy of an Orogen*, 1st ed.; Gebrüder Borntraeger: Berlin, Germany, 2002; p. 573.
29. Pipera, K.; Koroneos, A.; Soldatos, T.; Pécskay, Z.; Christofides, G. K/Ar mineral geochronology of the northern part of the Sithonia Plutonic Complex (Chalkidiki, Greece): Implications for its thermal history and geodynamic interpretation. *Geol. Carpathica* **2013**, *64*, 133–140. [CrossRef]
30. Siron, C.R.; Rhys, D.; Thompson, J.F.; Baker, T.; Veligrakis, T.; Camacho, A.; Dalampiras, L. Structural controls on porphyry Au-Cu and Au-rich polymetallic carbonate-hosted replacement deposits of the Kassandra mining district, Northern Greece. *Econ. Geol.* **2018**, *113*, 309–345. [CrossRef]
31. Gilg, H.A.; Frei, R. Chronology of magmatism and mineralization in the Kassandra mining area, Greece: The potentials and limitations of dating hydrothermal illites. *Geochim. Cosmochim. Acta* **1994**, *58*, 2107–2122. [CrossRef]
32. Pavlides, S.B.; Kondopoulou, D.P.; Kilias, A.T.; Westphal, M. Complex rotational deformations in the Serbo-Macedonian massif (north Greece): Structural and paleomagnetic evidence. *Tectonophysics* **1988**, *145*, 329–335. [CrossRef]
33. Lazos, I.; Pikridas, C.; Chatzipetros, A.; Pavlides, S. Determination of local active tectonics regime in central and northern Greece, using primary geodetic data. *Appl. Geomat.* **2020**, 1–15. [CrossRef]
34. Melfos, V.; Vavelidis, M.; Christofides, G.; Seidel, E. Origin and evolution of the Tertiary Maronia porphyry copper-molybdenum deposit, Thrace, Greece. *Miner. Depos.* **2002**, *37*, 648–668. [CrossRef]
35. Neubauer, F.; Heinrich, C.A. Geode ABCD working group Late Cretaceous and Tertiary geodynamics and ore deposit evolution of the Alpine-Balkan-Carpathian-Dinaride orogen. In *Mineral Exploration and Sustainable Development*; Eliopoulos, D., Ed.; Millpress: Rotterdam, The Netherlands, 2003; pp. 1133–1136.
36. Marchev, P.; Kaiser-Rohrmeier, M.; Heinrich, C.; Ovtcharova, M.; von Quadt, A.; Raicheva, R. Hydrothermal ore deposits related to post-orogenic extensional magmatism and core complex formation: The Rhodope Massif of Bulgaria and Greece. *Ore Geol. Rev.* **2005**, *27*, 53–89. [CrossRef]
37. Voudouris, P.; Melfos, V.; Spry, P.G.; Baker, T. Cenozoic porphyry-epithermal and other intrusion-related deposits in northeastern Greece: Geological, mineralogical and geochemical constraints. In *Eocene to Miocene Hydrothermal Deposits of Northern Greece and Bulgaria: Relationships Between Tectonic-Magmatic Activity, Alteration, and Gold Mineralization, Guidebook*; Voudouris, P.C., Siron, C.R., Márton, I., Eds.; Society of Economic Geologists: Littleton, CO, USA, 2016; Volume 54, pp. 43–82.
38. Siron, C.R.; Thompson, J.F.; Baker, T.; Darling, R.; Dipple, G. Origin of Au-rich carbonate-hosted replacement deposits of the Kassandra mining district, northern Greece: Evidence for Late Oligocene, structurally controlled, and zoned hydrothermal systems. *Econ. Geol.* **2019**, *114*, 1389–1414. [CrossRef]
39. Eldorado Gold Corporation Resources and Reserves. Available online: www.eldorado-gold.com/assets/resources-and-reserves/ (accessed on 5 May 2020).
40. Melfos, V.; Vavelidis, M.; Arikas, K. A new occurrence of argentopentlandite and gold from the Au-Ag-rich copper mineralisation in the Paliomylos area, Serbomacedonian Massif, Central Macedonia, Greece. *Bull. Geol. Soc. Greece* **2001**, *34*, 1065–1072. [CrossRef]
41. Tsirambides, A.; Filippidis, A. Sb-Bi-bearing metallogeny of the Serbomacedonian-Rhodope metallogenic belt (SRMB). *Bull. Geol. Soc. Greece* **2019**, *55*, 34–64. [CrossRef]
42. Melidonis, N. *Geological Mapping of Vathi, Kilkis*; Institute of Geology and Mineral Exploration (IGME): Athens, Greece, 1968; p. 20.
43. Thanasoulas, K. *Geophysical Study at the Volcanic Rocks Area of Vathi, Kilkis*; Institute of Geology and Mineral Exploration (IGME): Athens, Greece, 1979; p. 17.
44. Andronopoulos, B. *The Uranium Mineralization at Vathi, Kilkis*; Institute of Geology and Mineral Exploration (IGME): Athens, Greece, 1967; p. 12.
45. Filippidis, A.; Kougoulis, C.; Michailidis, K. Sr-bearing stilbite in a quartz monzonite from Vathi, Kilkis, Northern Greece. *Schweiz. Mineral. Petrogr. Mitt.* **1988**, *68*, 67–76.
46. Markoulis, M. *The Exploration Program at Vathi on Behalf of the Greek Atomic Energy Commission (EEAE) Targeting the Uraniferous Mineral Assemblages of the Region*; Institute of Geology and Mineral Exploration (IGME): Athens, Greece, 1970; p. 35.
47. Bakker, R.J. Package FLUIDS. Part 4: Thermodynamic modelling and purely empirical equations for H2O-NaCl-KCl solutions. *Mineral. Petrol.* **2012**, *105*, 1–29. [CrossRef]
48. Driesner, T.; Heinrich, C.A. The system H2O-NaCl. Part I: Correlations for molar volume, enthalpy, and isobaric heat capacity from 0 to 1000 degrees C, 1 to 5000 bar, and 0 to 1 X-NaCl. *Geochim. Cosmochim. Acta* **2007**, *71*, 4880–4901. [CrossRef]
49. Driesner, T. The system H2O-NaCl. Part II: Correlations for molar volume, enthalpy, and isobaric heat capacity from 0 to 1000 oC, 1 to 5000 bar, and 0 to 1 XNaCl. *Geochim. Cosmochim. Acta* **2007**, *71*, 4902–4919. [CrossRef]
50. Sillitoe, R.H. Ore-related breccias in volcanoplutonic arcs. *Econ. Geol.* **1985**, *80*, 1467–1514. [CrossRef]
51. Frost, B.R.; Frost, C.D. A geochemical classification for feldspathic igneous rocks. *J. Petrol.* **2008**, *49*, 1955–1969. [CrossRef]
52. Le Bas, M.J.; Le Maitre, R.W.; Streckeisen, A.; Zanettin, B. A chemical classification of volcanic rocks based on the total alkali-silica diagram. *J. Petrol.* **1986**, *27*, 745–750. [CrossRef]
53. Le Maitre, R.W.; Streckeisen, A.; Zanettin, B.; Le Bas, M.J.; Bonin, B.; Bateman, P. *Igneous Rocks: A Classification and Glossary of Terms: Recommendations of the International Union of Geological Sciences Subcommision on the Systematics of Igneous Rocks*, 2nd ed.; Cambridge University Press: Cambridge, UK, 2002; p. 256.

54. Taylor, S.R.; McLennan, S.M. *The Continental Crust; Its Composition and Evolution; an Examination of the Geological Record Preserved in Sedimentary Rocks*, 1st ed.; Blackwell Scientific Publication: Oxford, UK, 1985; p. 312.
55. Hedenquist, J.W.; Arribasm, A., Jr.; Reynolds, T.J. Evolution of an intrusion-centered hydrothermal system: Far Southeast-Lepanto porphyry and epithermal Cu-Au deposits, Philippines. *Econ. Geol.* **1998**, *93*, 373–404. [CrossRef]
56. Sillitoe, R.H. Porphyry Copper Systems. *Econ. Geol.* **2010**, *105*, 3–41. [CrossRef]
57. Dimitriadis, S. Callait (turquoise) in a weathered trachyte rock of Vathi Kilkis area. *Hell. J. Geosci.* **1973**, *25*, 328–332.
58. Sklavounos, S.; Ericsson, T.; Filippidis, A.; Michailidis, K.; Kougoulis, C. Chemical, X-ray and Mössbauer investigation of a turquoise from the Vathi area volcanic rocks, Macedonia, Greece. *Neues Jahrb. Mineral.* **1992**, *10*, 469–480.
59. Stavropodis, J.D.; Kotopouli, K. Autunite–a new uranium mineral for Greece. *Hell. J. Geosci.* **1972**, *24*, 424–432.
60. Stergiou, A.; Rentzeperis, P.J.; Sklavounos, S. Refinement of the crystal structure of metatorbernite. *Z. Krist.* **1993**, *205*, 1–7. [CrossRef]
61. Tarantola, A.; Diamond, L.W.; Stünitz, H.; Thust, A.; Pec, M. Modification of fluid inclusions in quartz by deviatoric stress. III: Influence of principal stresses on inclusion density and orientation. *Contrib. Mineral. Petrol.* **2012**, *164*, 537–550. [CrossRef]
62. Roedder, E. Fluid inclusions. *Rev. Miner.* **1984**, *12*, 644.
63. Goldstein, R.H.; Reynolds, T.J. *Systematics of Fluid Inclusions in Diagenetic Minerals*; Society for Sedimentary Geology: Broken Arrow, OK, USA, 1994; p. 199.
64. Diamond, L.W.; Tarantola, A. Interpretation of fluid inclusions in quartz deformed by weak ductile shearing: Reconstruction of differential stress magnitudes and predeformation fluid properties. *Earth Planet. Sci. Lett.* **2015**, *417*, 107–119. [CrossRef]
65. Shepherd, T.; Rankin, A.; Alderton, D. *A Practical Guide to Fluid Inclusion Studies*, 1st ed.; Blackie and Son: Glasgow, UK, 1985; p. 239.
66. Bodnar, R.J. Introduction to fluid inclusions. In *Fluid Inclusions: Analysis and Interpretation*; Samson, I.M., Anderson, A.J., Marshall, D.D., Eds.; Society for Sedimentary Geology: Broken Arrow, OK, USA, 2003; Volume 32, pp. 1–8.
67. Hemley, J.J.; Cygan, G.L.; Fein, J.B.; Robinson, G.R.; D'Angelo, W.M. Hydrothermal ore-forming processes in the light of studies in rock buffered systems: I. Iron-copper-zinc-lead sulfide solubility relations. *Econ. Geol.* **1992**, *87*, 1–22. [CrossRef]
68. Rabbia, O.M.; Hernández, L.B. Mineral chemistry and potential applications of natural-multi-doped hydrothermal rutile from porphyry copper deposits. In *Rutile: Properties, Synthesis and Application*; Low, I.K., Ed.; Nova Science Publishers: New York, NY, USA, 2012; pp. 209–228.
69. Brathwaite, R.L.; Simpson, M.; Faure, K.; Skinner, D. Telescoped porphyry Cu-Mo-Au mineralisation, advanced argillic alteration and quartz-sulphide-gold-anhydrite veins in the Thames District, New Zealand. *Miner. Depos.* **2001**, *36*, 623–640. [CrossRef]
70. Audétat, A.; Pettke, T.; Heinrich, C.A.; Bodnar, R.J. Special paper: The composition of magmatic-hydrothermal fluids in barren and mineralized intrusions. *Econ. Geol.* **2008**, *103*, 877–908. [CrossRef]
71. Zhang, Y.G.; Frantz, J.D. Determination of the homogenization temperatures and densities of supercritical fluids in the system NaCl-KCl-CaCl2-H2O using synthetic fluid inclusions. *Chem. Geol.* **1987**, *64*, 335–350. [CrossRef]
72. Zhong, J.; Chen, Y.J.; Pirajno, F.; Chen, J.; Li, J.; Qi, J.P.; Li, N. Geology, geochronology, fluid inclusion and H-O isotope geochemistry of the Luoboling porphyry Cu-Mo deposit, Zijinshan Orefield, Fujian Province, China. *Ore Geol. Rev.* **2014**, *57*, 61–77. [CrossRef]
73. Rusk, B.G.; Reed, M.H.; Dilles, J.H. Fluid inclusion evidence for magmatic-hydrothermal fluid evolution in the porphyry copper-molybdenum deposit at Butte, Montana. *Econ. Geol.* **2008**, *103*, 307–334. [CrossRef]
74. Muntean, J.L.; Einaudi, M.T. Porphyry-epithermal transition: Maricunga belt, northern Chile. *Econ. Geol.* **2001**, *96*, 743–772. [CrossRef]
75. Fournier, R.O. Hydrothermal processes related to movement of fluid from plastic into brittle rock in the magmatic-epithermal environment. *Econ. Geol.* **1999**, *94*, 1193–1211. [CrossRef]
76. Ulrich, T.; Gunther, D.; Heinrich, C.A. Gold concentrations of magmatic brines and the metal budget of porphyry copper deposits. *Nature* **1999**, *399*, 676–679. [CrossRef]
77. Heinrich, C.A. The physical and chemical evolution of low-salinity magmatic fluids at the porphyry to epithermal transition: A thermodynamic study. *Miner. Depos.* **2005**, *39*, 864–889. [CrossRef]
78. Voudouris, P.; Melfos, V.; Spry, P.G.; Kartal, T.; Schleicher, H.; Moritz, R.; Ortelli, M. The Pagoni Rachi/Kirki Cu-Mo-Re-Au-Ag-Te deposit, northern Greece: Mineralogical and fluid inclusion constraints on the evolution of a telescoped porphyry-epithermal system. *Can. Miner.* **2013**, *51*, 411–442. [CrossRef]
79. Bonin, B.; Sekkal, A.A.; Bussy, F.; Ferrag, S. Alkali-calcic and alkaline post-orogenic (PO) granite magmatism: Petrologic constraints and geodynamic settings. *Lithos* **1998**, *45*, 45–70. [CrossRef]
80. Davidson, J. Strontium in igneous rocks. In *Encyclopedia of Geochemistry*, 1st ed.; Marshall, C.P., Fairbridge, R.W., Eds.; Springer Science and Business Media: Berlin, Germany, 1999; pp. 599–600.
81. Richards, J.P. Magmatic to hydrothermal metal fluxes in convergent and collided margins. *Ore Geol. Rev.* **2011**, *40*, 1–26. [CrossRef]
82. Richards, J.P.; Mumin, A.H. Magmatic-hydrothermal processes within an evolving Earth: Iron oxide-copper-gold and porphyry Cu±Mo±Au deposits. *Geology* **2013**, *41*, 767–770. [CrossRef]
83. Rice, C.M.; Harmon, R.S.; Shepherd, T.J. Central City, Colorado; the upper part of an alkaline porphyry molybdenum system. *Econ. Geol.* **1985**, *80*, 1769–1796. [CrossRef]

84. Menant, A.; Jolivet, L.; Tuduri, J.; Loiselet, C.; Bertrand, G.; Guillou-Frottier, L. 3D subduction dynamics: A first-order parameter of the transition from copper-to gold-rich deposits in the eastern Mediterranean region. *Ore Geol. Rev.* **2018**, *94*, 118–135. [CrossRef]
85. Loucks, R.R. Distinctive composition of copper-ore forming arc magmas. *Aust. J. Earth Sci.* **2015**, *61*, 5–16. [CrossRef]
86. Candela, P.A.; Holland, H.D. A mass transfer model for copper and molybdenum in magmatic hydrothermal systems: The origin of porphyry-type ore deposits. *Econ. Geol.* **1986**, *81*, 1–19. [CrossRef]
87. Rowins, S.M. Reduced porphyry copper-gold deposits: A new variation on an old theme. *Geology* **2000**, *28*, 491–494. [CrossRef]
88. Cao, K.; Yang, Z.M.; Mavrogenes, J.; White, N.C.; Xu, J.F.; Li, Y.; Li, W.K. Geology and genesis of the giant Pulang porphyry Cu-Au district, Yunnan, southwest China. *Econ. Geol.* **2019**, *114*, 275–301. [CrossRef]